

1 **Full title:** Targeted photothrombotic stroke leads to disruptions in neurovascular coupling
2 **Short title:** Ischemic stroke leads to neurovascular uncoupling

3 **Authors**

4 Smrithi Sunil^{1,*}, John Jiang¹, Shashwat Shah¹, Sreekanth Kura¹, Kivilcim Kilic¹, Sefik Evren
5 Erdener², Cenk Ayata³, Anna Devor^{1,4}, David A. Boas^{1,+}

6

7 **Affiliations**

8 ¹Department of Biomedical Engineering, Boston University, Boston, MA 02215

9 ²Institute of Neurological Sciences and Psychiatry, Hacettepe University, Ankara, Turkey

10 ³Departments of Neurology and Radiology, Massachusetts General Hospital, Boston, MA 02114

11 ⁴Athinoula A. Martinos Center for Biomedical Imaging, Massachusetts General Hospital, Boston,
12 MA 02114

13 [*smrithi.x.sunil@gmail.com](mailto:smrithi.x.sunil@gmail.com)

14 [+dboas@bu.edu](mailto:dboas@bu.edu)

15

16 **Teaser**

17 Acute ischemic stroke leads to neurovascular uncoupling and the extent of early recoupling
18 predicts sensorimotor recovery.

19

20 **Abstract**

21 Functional neuroimaging, which measures hemodynamic responses to brain activity, has great
22 potential for monitoring stroke patients. However, the neurophysiological interpretations of these
23 hemodynamic signals remain a challenge as the stroke is likely to alter both neural activity and
24 neurovascular coupling. To address this challenge, we simultaneously captured neural activity,
25 through fluorescence calcium imaging, and hemodynamics, through intrinsic optical signal
26 imaging, during longitudinal stroke recovery. We found that photothrombotic stroke to
27 somatosensory forelimb region altered neurovascular coupling in the acute phase (2 days and 1
28 week post-stroke) within the affected forelimb and peri-infarct regions. Neurovascular coupling
29 was reestablished in the chronic phase (4 weeks post-stroke), and acute recovery of neurovascular
30 coupling predicted sensorimotor function. Stroke also resulted in increases in the power of global
31 brain oscillations, which showed distinct patterns between calcium and hemodynamics. Increased
32 calcium excitability in the contralesional hemisphere was associated with increased

33 intrahemispheric connectivity. Additionally, acute increases in hemodynamic oscillations were
34 associated with improved sensorimotor outcomes.

35

36 **Introduction**

37 An ischemic stroke occurs due to interruption of blood flow caused by thrombosis or embolism of
38 a blood vessel, which leads to a reduction or complete loss of blood supply to downstream areas.
39 Loss of blood supply causes a starved oxygen environment and leads to cellular damage within
40 minutes and ultimately to sensorimotor and cognitive impairments^{1,2}. A majority of stroke patients
41 survive the incident, however, most survivors are compromised in work capacity, the extent of
42 which varies across patients from mild to severe impairments³. Some spontaneous recovery is
43 typically seen in most patients in the months following injury and most post-stroke recovery
44 currently relies heavily on rehabilitative treatments⁴⁻⁶.

45 Functional neuroimaging methods, such as functional magnetic resonance imaging (fMRI)
46 and functional near-infrared spectroscopy (fNIRS), which measure the hemodynamic response to
47 brain activity, have the potential for being valuable tools for monitoring and managing the recovery
48 and treatment of stroke patients both in the acute and chronic phases of stroke recovery⁷⁻⁹.
49 However, the hemodynamic responses post-stroke are almost always altered relative to those seen
50 in healthy individuals. Blood-oxygen-level-dependent fMRI (BOLD-fMRI) studies have revealed
51 that task-related cortical responses following stroke undergo pronounced alterations in amplitude
52 and spatial extent of the BOLD signal in both the ipsilesional and the contralesional hemispheres⁹⁻
53 ¹¹. Additionally, studies assessing resting-state functional connectivity obtained with MRI (fc-
54 MRI) have shown that inter-hemispheric connections are altered in the early acute phase of stroke

55 in humans^{12,13}. Whether these hemodynamic response alterations reflect the underlying differences
56 in neural function or simply a result of injury to the vasculature is still under active investigation.
57 In other words, we do not know the effect of stroke on neurovascular coupling and thus are limited
58 in our ability to use these valuable neuroimaging tools to study functional recovery in stroke
59 survivors.

60 Neurovascular coupling (NVC) has been studied extensively in healthy subjects and there
61 is a large body of evidence suggesting that neural activity is closely related to cerebral blood flow
62 (CBF) and oxygen metabolism^{14,15}. This tight coupling between neural activity and hemodynamics
63 forms the basis of modern neuroimaging techniques that use the cerebrovascular changes caused
64 by neural activation to map changes in function in the behaving human brain¹⁶. While NVC is
65 maintained in the healthy brain, brain pathologies such as traumatic brain injury, Alzheimer's
66 disease, and stroke may lead to disruptions in the interactions between neural activity and CBF,
67 leading to neurovascular uncoupling, thereby confounding interpretations of neuroimaging
68 results^{17,18}. Additionally, the effect of stroke on NVC has received limited attention and sometimes
69 led to conflicting results^{9,19,20}. Thus, there is a need for preclinical stroke models to evaluate the
70 functional aspects of neurovascular recovery and to use these findings to improve the
71 interpretations of human neuroimaging studies.

72 Preclinical animal models of stroke have been used extensively over the last few decades
73 to understand the mechanisms involved in stroke recovery from molecular and cellular changes to
74 large scale functional network reorganizations²¹⁻²³. On a mesoscopic level, studies performing *in*
75 *vivo* calcium fluorescence imaging of neural activity have shown activation reorganization and
76 functional remapping of the affected brain regions in the peri-infarct zone longitudinally, bearing
77 on physiological processes underlying the evolution of stroke in humans²⁴⁻²⁷. Additionally,

78 intrinsic optical signal imaging (IOSI) has been used to assess global changes using resting state
79 functional connectivity analysis and also local changes in response to functional activation^{28,29}. To
80 improve interpretations of human functional neuroimaging studies and to understand the
81 underlying physiology that gives rise to the observed hemodynamic signals we need to obtain
82 simultaneous measures of neural and hemodynamic parameters post-stroke. Moreover, these
83 measures need to be obtained on a mesoscopic scale to understand both the local and global
84 changes that result due to stroke, as well as cover the entire longitudinal recovery phase to capture
85 both acute and chronic time points.

86 Prior work on functional recovery following ischemic stroke has focused either just on
87 neural or hemodynamic activity changes or just the acute or chronic phase and to the best of our
88 knowledge these measures have not yet been integrated to study neurovascular coupling during
89 stroke recovery^{24,28-31}. In this paper, we study the relationships between neural and hemodynamic
90 activity in the affected and unaffected hemispheres during longitudinal stroke recovery. We have
91 previously established an optimized stroke model that more closely mimicked the physiology of a
92 human stroke by inducing a stroke in an awake animal, occluding a single arteriole, and eliciting
93 a distinct core and peri-infarct region. Here, we show that our optimized stroke model together
94 with wide-field neural calcium and hemodynamic imaging can be used to monitor neurovascular
95 coupling longitudinally. Our results suggest that acute stroke leads to neurovascular uncoupling as
96 assessed through activity correlations and the hemodynamic response function. This uncoupling
97 was capable of spontaneous re-coupling, which depended on the extent of initial acute uncoupling.
98 Furthermore, the extent of neurovascular re-coupling was associated with improved sensorimotor
99 outcomes.

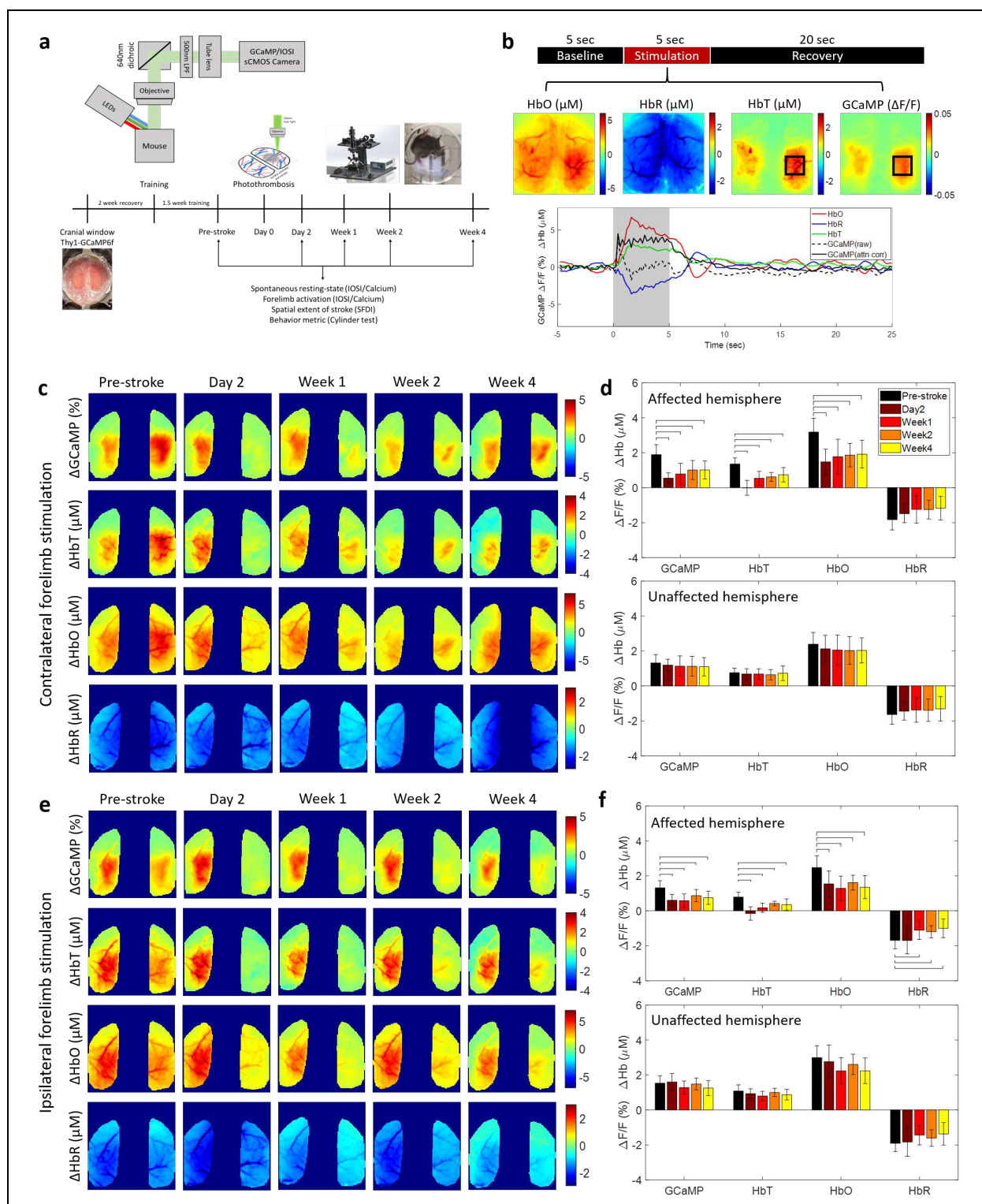
100

101 **Results**

102 **Wide-field fluorescence and intrinsic optical signal imaging can simultaneously follow
103 changes in neural calcium and hemodynamic activity after stroke**

104 Neurovascular coupling has been studied extensively in healthy subjects in both humans and
105 animal models. In rodents, wide-field fluorescence calcium and intrinsic optical hemodynamic
106 signals have been imaged simultaneously to investigate the baseline relationships between neural
107 activity and blood flow^{32,33}. Imaging calcium dynamics using GCaMP has been used extensively
108 over the last decade as a correlate and reliable metric of neural activity^{34,35}. Here, we first
109 implemented these techniques to show that wide-field optical imaging can be used to investigate
110 the differential effects of stroke on neural calcium dynamics and cerebral blood volume assessed
111 with changes in the concentration of oxy and deoxy hemoglobin (HbO and HbR respectively). Fig
112 1a shows a simplified schematic of the imaging system and the experimental timeline. We first
113 assessed alterations to evoked responses during sensory stimulation after stroke. Sensory
114 stimulation using air-puff to the forelimb was performed in a block design paradigm (Fig 1b) and
115 included 5 sec of baseline, followed by 5 sec of 3 Hz stimulation, followed by 20 sec of rest before
116 the next trial. Each trial was repeated 20 times in one session. Fig 1b shows an example of the
117 spatial maps and time-course of stimulus induced response in a healthy mouse. The raw GCaMP
118 fluorescence signal was corrected for hemodynamic crosstalk using a modified attenuation
119 estimation method prior to analysis^{32,36} (Fig 1b, Supplementary Fig 1). Unilateral photothrombotic
120 stroke to the forelimb somatosensory cortex of the right hemisphere led to a significant suppression
121 of the evoked calcium and hemodynamic responses to air-puff stimulation of the contralateral
122 (affected) forelimb within the affected hemisphere, while the responses in the unaffected
123 hemisphere were preserved (Fig 1c,d). The largest suppression of the response occurred 2 days

124 post-stroke with a slow return of the response by 4 weeks, albeit still suppressed compared to pre-
125 stroke. At day 2 after stroke, GCaMP showed a 70% reduction in the response. At the same time,
126 total hemoglobin (HbT) and HbO showed a 100% and 45% reduction in response, respectively,
127 compared to pre-stroke baseline (Supplementary Fig 2a). By 4 weeks after stroke the responses
128 within the affected hemisphere had returned to 50% of the pre-stroke value. Evoked responses to
129 forelimb air-puff stimulation of the unaffected forelimb did not exhibit significant alterations in
130 the contralateral (unaffected) hemisphere, however, the affected hemisphere showed suppressed
131 responses (Fig 1e,f). Once suppressed, the affected hemisphere did not recover either GCaMP or
132 hemodynamic responses to ipsilateral (unaffected) forelimb stimulation even at 4 weeks
133 (Supplementary Fig 2b). Spatiotemporal maps of responses during baseline, stimulation, and
134 recovery at each time point are shown in Supplementary Fig 3 for the same mouse shown in Fig
135 1c,e. Knowing the co-evolution of neural and hemodynamic responses can aid in better
136 interpretations of the alterations observed in the hemodynamic fMRI signals after stroke. The
137 results here show that wide-field fluorescence and intrinsic optical signal imaging following
138 photothrombotic stroke are sensitive measures that allow the longitudinal monitoring of these
139 neural and hemodynamic signals.



140

141 **Figure 1: Simultaneous calcium and hemodynamic imaging post-stroke.** (a) Simplified
 142 imaging schematic and experimental timeline. (b) Top: Block design of each trial in a stimulation
 143 session, middle: trial averaged spatial maps of HbO, HbR, HbT, and corrected GCaMP, during 5
 144 sec of air-puff stimulation to the left forelimb, bottom: trial averaged time course of each

145 measurement, note that raw uncorrected GCaMP drops immediately following the rise of the
146 hemodynamic response and corrected GCaMP shows elevated responses through the full
147 stimulation period. (c) Trial-averaged spatial maps of calcium and hemodynamics showing
148 magnitude of the response during 5-sec stimulation of the contralateral (affected) forelimb at each
149 time point before and after stroke in one example mouse. (d) Response magnitudes during affected
150 forelimb stimulation for all mice (n=12) in the affected (top) and unaffected (bottom) hemispheres,
151 histograms are mean \pm std. (e) Same as in (c) during stimulation of the ipsilateral (unaffected)
152 forelimb. (f) Same as in (d) during stimulation of the ipsilateral (unaffected) forelimb. Bars in (d)
153 and (f) indicate significance of $p < 0.05$.

154

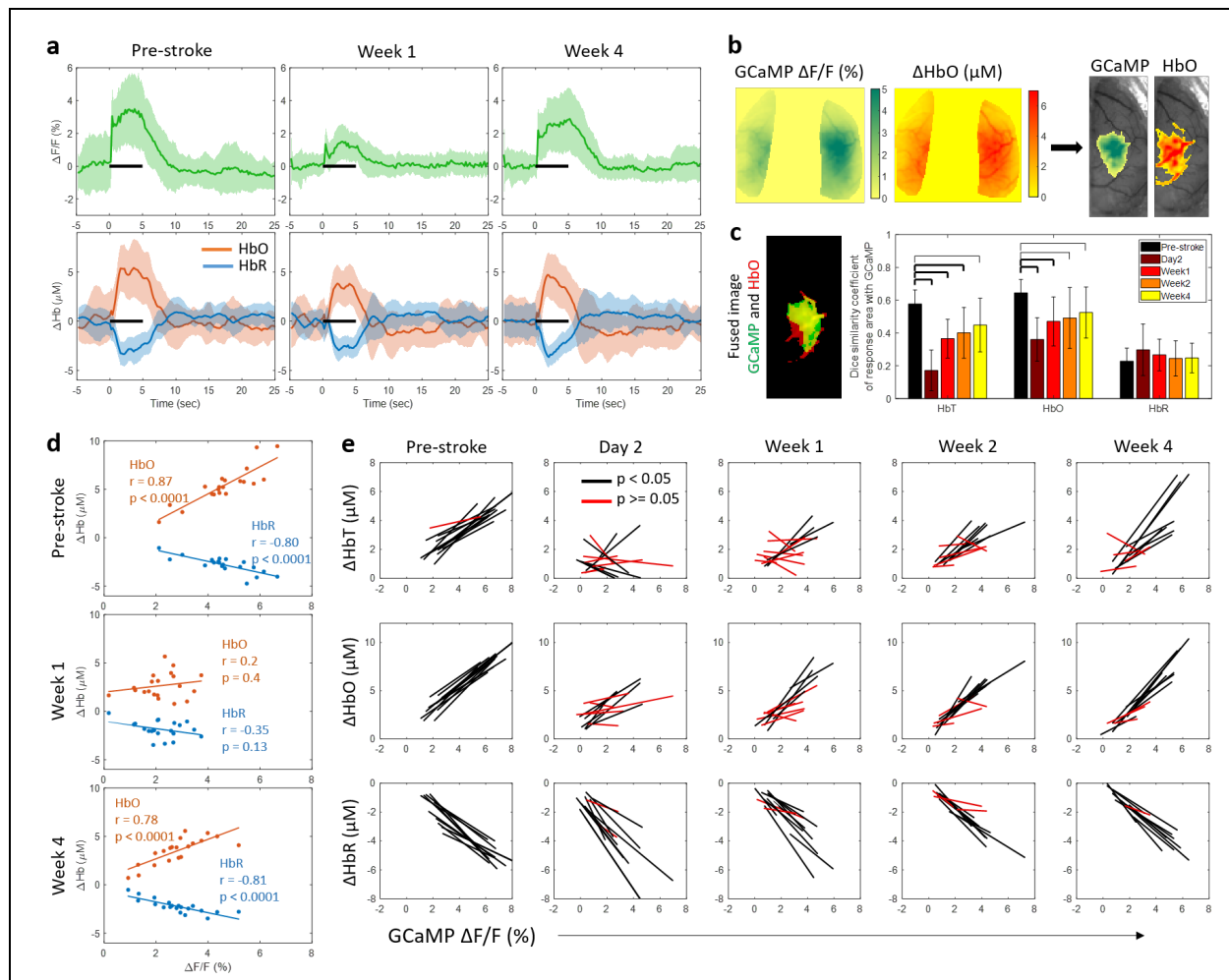
155 **Acute stroke leads to alterations in the correlation between evoked calcium and**
156 **hemodynamic responses**

157 To evaluate NVC, we examined whether aspects of the observed hemodynamic responses were
158 correlated with the underlying calcium activity during sensory stimulation of the impaired
159 forelimb. Fig 2a shows the trial-averaged mean and standard deviation of the time course of
160 calcium, measured as a percent change in fluorescence (top row), and change in HbO and HbR,
161 measured in μM (bottom row), averaged from all pixels within the affected hemisphere at pre-
162 stroke, 1 week, and 4 weeks post-stroke. Spatial response maps, obtained during the 5-sec
163 stimulation period, were then thresholded at each time point to 75% of the peak response and all
164 pixels that lie above that threshold were used for correlation analysis (Fig 2b). We first examined
165 the similarity in the response areas between the evoked calcium response and hemodynamic
166 measures. Similarity was calculated using the Dice coefficient, which provides a measure of the
167 percent overlap, or union, of two images (Fig 2c). HbT and HbO showed high overlap (60%) with
168 GCaMP before the stroke, indicating that GCaMP and hemodynamic responses were spatially
169 localized, while HbR had a weaker spatial overlap with GCaMP (20%). Within the ipsilesional
170 hemisphere, HbT and HbO showed a significant reduction in the spatial overlap with GCaMP
171 across all time points after stroke, with a larger reduction in the acute time points of day2 and

172 week1 compared to chronic time points. In contrast, the overlap between HbR and GCaMP was
173 not significantly altered. Similarity between GCaMP and hemodynamic response maps in the
174 contralateral hemisphere were not significantly altered after stroke (Supplementary Fig 5a).

175 Next, we calculated the average magnitude of the response during 5 seconds of air-puff
176 stimulation within all pixels above 75% of peak activation. We then correlated the magnitude of
177 the GCaMP response to the magnitude of the HbO and HbR responses for each stimulus trial. Fig
178 2d shows an example pre- and post-stroke dataset from one mouse; each dot in the scatter plot
179 represents data from one trial within a block of 20 trials. There was high correlation between the
180 evoked GCaMP responses and HbO, as well as GCaMP and HbR, prior to stroke, demonstrating
181 healthy coupling between neural activity and hemodynamics. The correlation was lost 1 week after
182 stroke following a reestablishment by week 4. This evolution of correlation was seen across the
183 cohort of animals (Fig 2e). Both HbT and HbO showed significant loss in correlation with GCaMP
184 in the acute phase, implying that calcium responses in the acute phase were not necessarily
185 represented in the observed hemodynamic response. However, this loss in correlation could also
186 be due to the small amplitudes of the signal, which can result in larger noise and thus low
187 correlation. Additionally, those mice that had a residual loss of correlation at week 4 compared to
188 those that fully recovered, also had a worse correlation between GCaMP and HbT/HbO responses
189 in the acute phase (Supplementary Fig 4). The correlation between calcium and hemodynamic
190 responses in the contralateral hemisphere was preserved throughout the recovery period
191 (Supplementary Fig 5b).

192



193

194 **Figure 2: Correlation between evoked calcium and hemodynamic responses.** (a) Trial-
195 averaged time-course showing mean (\pm std) of GCaMP (top) and HbO and HbR (bottom) for all
196 pixels within the affected hemisphere at the pre-stroke baseline, 1 week, and 4 weeks post-stroke.
197 Note the drop in response to stimulation (black bar) at week 1. (b) Threshold algorithm applied to
198 GCaMP and Hb responses. (c) Overlap between the response area of GCaMP and HbO, left: single
199 trial fused image for reference, GCaMP is green, HbO is red, and overlap region is yellow, right:
200 Dice similarity coefficients across all mice (n=12) and time points. Thick bars: p<0.01, thin bars:
201 p<0.05. (d) Correlation of response magnitudes between GCaMP and HbO and HbR for one mouse
202 at pre-stroke, week 1, and week 4. Inset numbers represent correlation value and significance of
203 fit. (e) Correlation of calcium and hemodynamics across all mice (n=12) over all time points; each
204 line represents one mouse. Black lines represent significant correlation and red lines represent no
205 significance.

206

207

208 **Acute stroke distorts the shape of the neurovascular response within the peri-infarct zone**
209 **that is restored in the chronic phase**

210 The next question we asked was whether the shape of stimulus-induced neurovascular response
211 was preserved across the acute and chronic phases of stroke recovery. To that end, we estimated a
212 hemodynamic response function (HRF) (or impulse response function (IRF)), which is the kernel
213 that, when convolved with the GCaMP signal, provides an estimate of the hemodynamic activity.
214 Linear least-squares deconvolution was used to estimate the HRF from the data as established
215 previously^{32,37}. First, we validated the method using the baseline (pre-stroke) data. We calculated
216 the HRF using the entire time-course for all pixels that responded to forelimb air-puff stimulation
217 (>75% of peak response) in HbT maps (Fig 3a, top). We observed the expected and characteristic
218 shape of the HRF, a post-stimulus overshoot, peaking at approximately 1 sec following
219 stimulation, followed by an undershoot, as reported previously^{32,38}. Next, we applied the same
220 procedure to data collected 2 days following stroke using the same brain region that originally
221 responded to forelimb stimulation. This analysis resulted in a distinctly altered HRF, suggesting a
222 disruption to neurovascular coupling (Fig 3a, bottom). Fig 3b shows the time-course of four
223 individual stimulation trials; the measured GCaMP signal is overlaid with the measured HbT and
224 estimated HbT, where the estimated HbT was obtained by convolving the GCaMP signal with the
225 time-point specific HRF kernel. Pre-stroke, the measured and estimated HbT showed good overlap
226 (Fig 3b, top), while at day 2 after stroke the overlap was poor (Fig 3b, bottom). Additionally, at
227 day 2 after stroke, there was no response to stimulation, and we observed large oscillations in the
228 measured hemodynamic signal. A Pearson's correlation coefficient was calculated between the
229 measured and estimated HbT signal at each pixel for both hemispheres of the brain (Fig 3c), and
230 we observed high correlation across the somatosensory cortex in both hemispheres before the

231 stroke (Fig 3c, top). From this we can conclude that hemodynamic activity was coupled to the
232 underlying calcium activity prior to stroke. Regions closer to motor cortex showed lower
233 correlation compared to regions within sensory cortex. Higher correlation in the sensory cortex
234 could be due to the presence of air-puff stimulus, which could be driving both calcium and
235 hemodynamic responses and strengthening our observation of neurovascular coupling. This
236 hypothesis could be validated by comparing the HRF and correlation obtained during resting-state
237 and sensory stimulation sessions. Prior work has shown that neural activity is more weakly
238 correlated to hemodynamics during resting state and this can also be validated from our data
239 (Supplementary Fig 6)³⁹. Our resting-state data still show a relatively high correlation, which could
240 be due to natural behavior of the mouse, such as whisking and grooming, driving cortical activity.
241 At day 2 after stroke there was a loss in correlation between the measured and predicted HbT as
242 indicated by drop in the Pearson's correlation coefficient (Fig 3c, bottom).

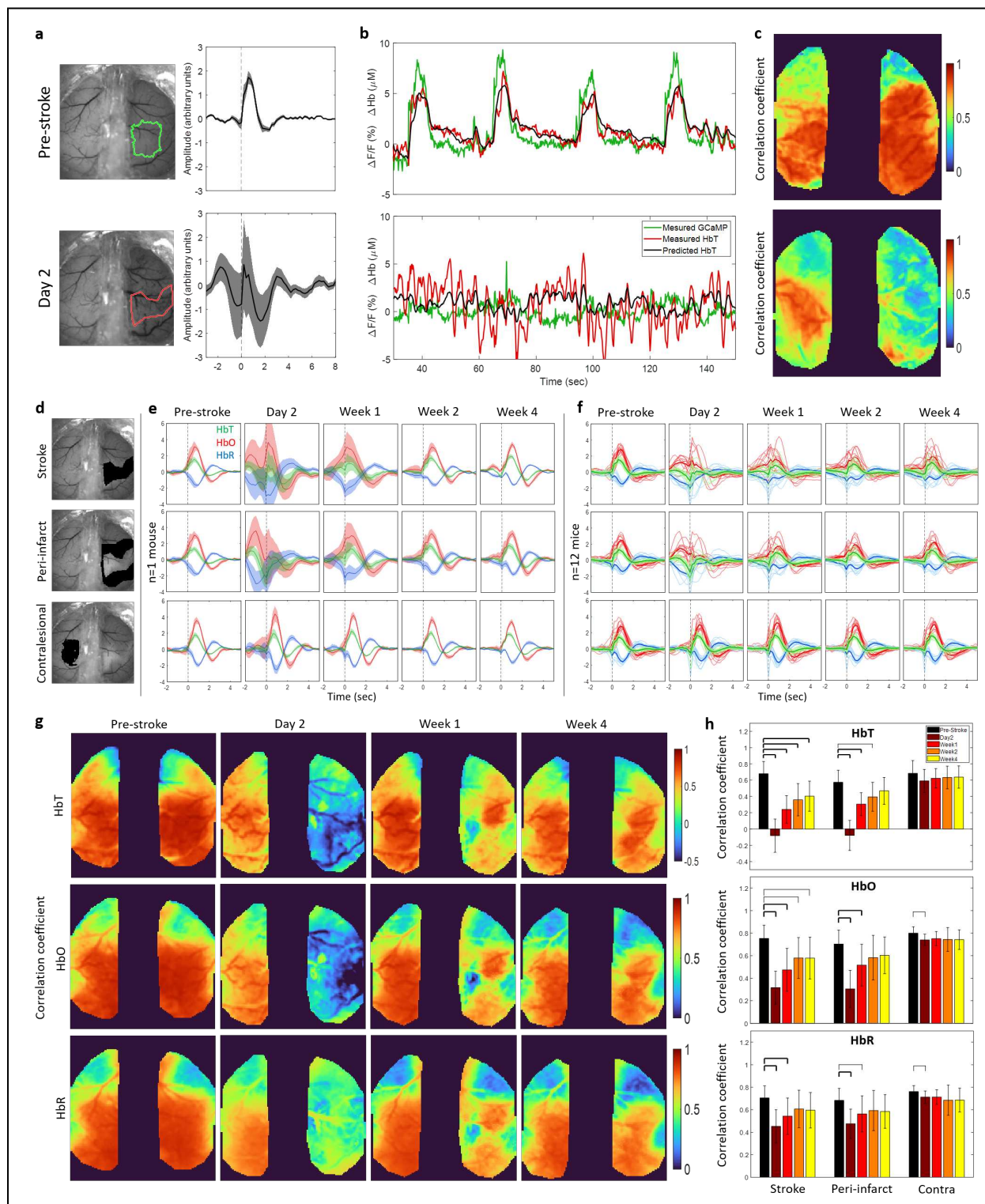
243 The same convolution model was applied to calcium and hemodynamic data to estimate
244 the HRF post-stroke across all animals and time points. The post-stroke HRF was calculated for
245 the stroke core, the peri-infarct region, which included all the pixels within 0.5 mm from the stroke
246 core boundary, and the contralesional forelimb region. The HRF was also calculated for HbO and
247 HbR in addition to HbT. Fig 3d shows an example mouse where the stroke core, peri-infarct, and
248 contralesional forelimb are highlighted in black. We then followed the evolution of the HRF for
249 each hemodynamic measure after stroke. Fig 3e shows the mean and standard deviation of the
250 HRF for one example mouse. We observed a significant deviation in the HRF within the stroke
251 core and peri-infarct region in the acute phase of recovery. Following the acute phase, the chronic
252 phase showed a recovery in the HRF. The contralesional HRF remained largely unaffected by the
253 stroke. Similar trends were observed across all animals (Fig 3f), where acute stroke resulted in

254 deviation of the HRF in the core and peri-infarct, while the contralesional hemisphere was
255 unaffected. In the chronic phase the HRF showed better recovery of the shape, with respect to pre-
256 stroke HRF, in the peri-infarct region. The HRF within the stroke core continued to show deviation
257 in some animals.

258 Here, we describe deviation of the HRF in terms of the qualitative similarity of shape to
259 the pre-stroke HRF. However, even if the shape of the HRF is different, it could still be used to
260 accurately predict hemodynamics. Therefore, we next tested the ability of the HRF at each time
261 point to predict hemodynamics. Supplementary Fig 7a shows a pixel-by-pixel map of the Pearson's
262 correlation coefficient for one example mouse for all three hemodynamic measures before and
263 after stroke. We observed a clear drop in correlation coefficient within the affected hemisphere,
264 specifically in day 2. Over time, through the recovery period, we observed some return of
265 correlation between the measured and predicted hemodynamics. The correlation coefficient was
266 quantified across all mice in the stroke core, peri-infarct, and contralesional forelimb region
267 (Supplementary Fig 7b). The stroke core showed a significant reduction in correlation coefficient
268 across all time points compared to before stroke, implying that the hemodynamic response
269 captured the underlying neural activity significantly worse compared to pre-stroke. Additionally,
270 this shows that the deviation in shape of the HRF was also associated with a lack of correlation
271 between measured and predicted hemodynamics. There was also a significant decrease in the
272 ability of the neurovascular coupling model to capture the hemodynamics from the measured
273 GCaMP signal within the peri-infarct region in the acute phase of day 2 and week 1. However,
274 unlike the stroke core, the peri-infarct showed recovery in terms of reestablishing the correlation
275 between the measured and predicted hemodynamics in the chronic phase, which was also
276 associated with a return of the HRF shape to the pre-stroke shape.

277 From the shape of the HRF we can clearly see that the neurovascular coupling model is not
278 behaving as expected during day 2 and week 1. Most notably, we see that the HRF is not flat prior
279 to stimulus onset at time = 0 as we would expect. We have provided more flexibility in our model
280 by allowing it to use GCaMP events that have not happened yet to find the best fit. In the pre-
281 stroke case this negative time region is a flat line at zero indicating that future GCaMP events have
282 no influence on the current hemodynamics, as expected. However, after stroke, specifically at day
283 2 and week 1, the HRF is no longer flat before time zero. While it is physiologically not possible
284 for future GCaMP events to influence current hemodynamics, this deviation in the HRF indicates
285 that there are possibly additional dynamics that are not captured by the original model and the
286 model is just trying to find the best fit with the given data. We can overcome this limitation and
287 test deviations in neurovascular coupling by testing how well we are able to predict the post-stroke
288 hemodynamics with the pre-stroke HRF, since we know that the pre-stroke HRF is behaving as
289 expected. To test this, we calculated the mean HRF for each mouse from pre-stroke “healthy” data
290 and convolved it with the post-stroke GCaMP time-course and obtained the correlation with this
291 predicted and measured hemodynamics (Fig 3g). Similar to when we used the time-point specific
292 HRF, there was a significant drop in correlation within the stroke and peri-infarct regions in the
293 acute phase and a recovery within the peri-infarct region in the chronic phase when using the pre-
294 stroke “healthy” HRF (Fig 3h). Unlike the time-point specific HRF correlations (Supplementary
295 Fig 7a, 7b), the healthy HRF correlations with post-stroke data showed virtually no correlation
296 between the measured and predicted HbT and only a small correlation in HbO at day 2. This
297 suggests that the neurovascular coupling model described for healthy brains is not sufficient to
298 describe post-stroke neurovascular dynamics during the acute phase. The stroke core continued to

299 show poor correlation even in the chronic phase at week 4 but the peri-infarct region exhibited a
 300 recovery.



301

302 **Figure 3: Neurovascular coupling with linear least-squares deconvolution.** (a) Hemodynamic
303 response function (HRF) before (top) and 2 days after stroke (bottom) in the forelimb and stroke
304 regions outlined in green and red respectively. (b) Time course of 4 stimulation trials showing
305 measured GCaMP signal overlaid with measured HbT and predicted HbT, obtained by convolving
306 the GCaMP signal with the HRF kernel, at pre-stroke and day 2 for the regions outlined in (a). (c)
307 Pearson's correlation coefficient for measured HbT and predicted HbT for pre-stroke (top) and 2
308 days after stroke (bottom). (d) Regions used to extract HRF in (e) and (f). (e) HRF obtained by
309 deconvolution model for HbT, HbO, and HbR, for one example mouse at each time point before
310 and after stroke. Note the deviation in HRF compared to pre-stroke in the acute phase within the
311 stroke and peri-infarct, and a return to pre-stroke HRF at week 4. (f) Same as in (e) for all mice
312 (n=12). Each line represents the HRF for one mouse. (g) Pixel-by-pixel Pearson's correlation
313 coefficient between measured and predicted HbT (top), HbO (middle), and HbR (bottom).
314 Predicted HbX is obtained by convolving the GCaMP signal at each time point with a mean HRF
315 obtained from pre-stroke data. (h) Pearson's correlation coefficient quantified across all mice
316 within the stroke core, peri-infarct, and contralesional forelimb region. Thick bars: p<0.01, thin
317 bars: p<0.05. Note the sustained reduction of correlation coefficient within the stroke core but
318 recovery within the peri-infarct for HbT and HbO.

319

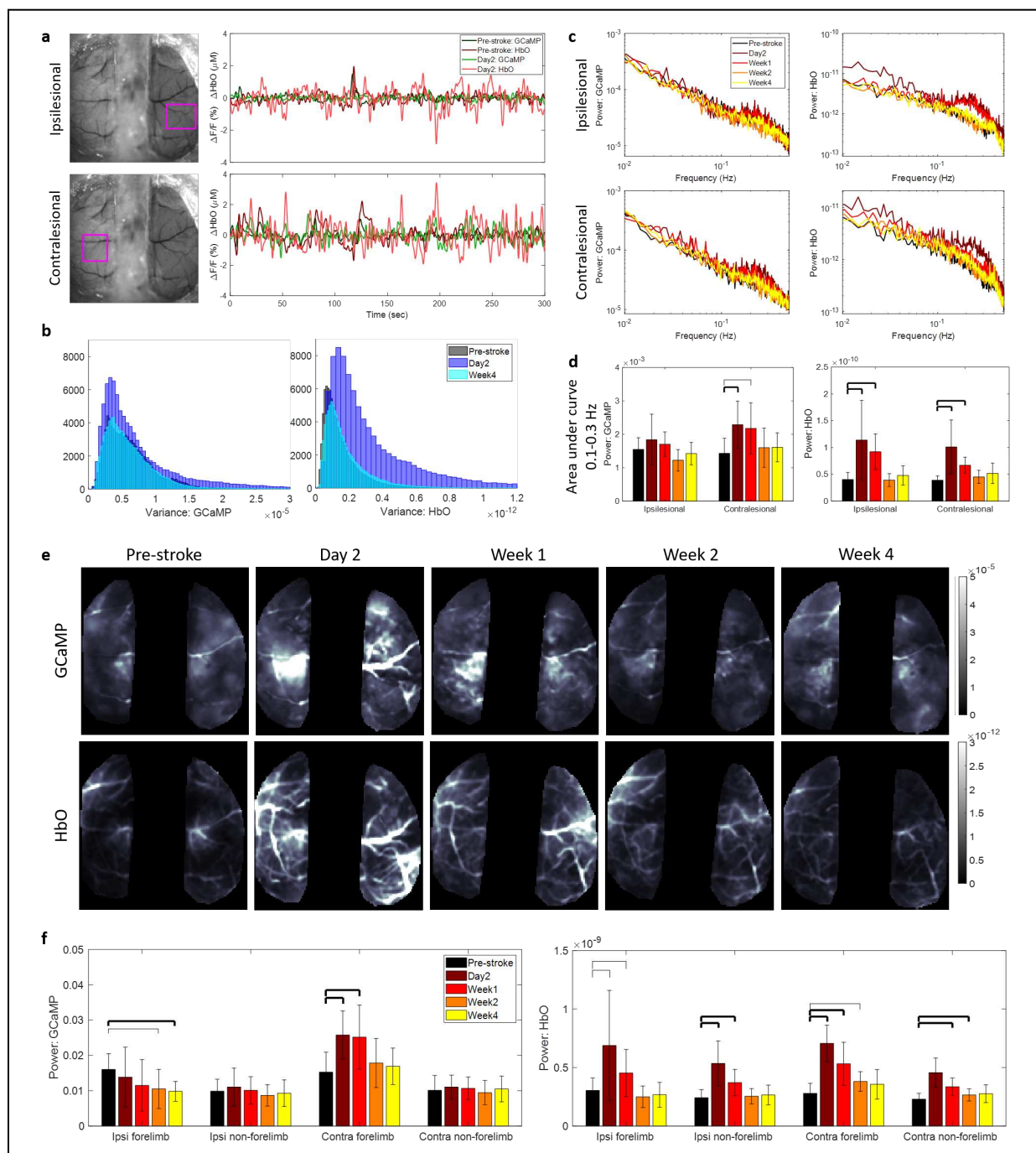
320 **Acute stroke leads to increases in power of global brain oscillations**

321 Stroke is known to have a profound effect not only on the local network but also on the
322 contralesional and subcortical networks of the brain. Additionally, in our neurovascular coupling
323 analysis we observed an increase in oscillatory dynamics in the hemodynamic signal. Through our
324 wide-field imaging approach we can assess the effect of stroke on both hemispheres of the brain
325 during resting-state. To assess brain-wide variations in the signals we first investigated the overall
326 change to signal patterns. Fig 4a shows the resting-state time-courses of GCaMP and HbO signals
327 at pre-stroke and 2 days post-stroke within the ipsilesional peri-infarct (Fig 4a, top) and the
328 contralesional forelimb regions (Fig 4a, bottom) that was filtered at 0.009-0.4Hz, which covers the
329 low and high frequency hemodynamic signal ranges used in prior work⁴⁰. A feature of note here
330 is the increase in amplitude of the HbO signal at day 2 in the ipsilesional hemisphere (light red line
331 in Fig 4a top) compared to pre-stroke, but an increase in amplitude of both the HbO and GCaMP
332 signal at day 2 within the contralesional hemisphere. We validated this increase in amplitude by

333 calculating the variance in the overall signal (Fig 4b). GCaMP showed only minor alterations in
334 variance while HbO showed a large increase in the variance of its signal at day 2, which was
335 resolved by week 4. To address whether this increase in the amplitude of the signal was an increase
336 in the power of the signal across all frequencies or specific to a particular frequency. We calculated
337 the power spectrum of the GCaMP and hemodynamic signal within the affected and unaffected
338 hemisphere (Fig 4c). There was an overall increase in power across all frequencies at 2 days after
339 stroke in the HbO signal of the ipsilesional hemisphere. Moreover, there was a significant increase
340 in power of the hemodynamic signal at 2 days and 1 week after stroke at specifically around 0.25
341 Hz within the ipsilesional hemisphere. The contralesional hemisphere on the other hand showed
342 increased power at 0.25 Hz at day 2 after stroke in both GCaMP and hemodynamics. Fig 4d shows
343 the area under the curve in the frequency range of 0.1-0.3 Hz, where the largest increase in power
344 was observed. This increase in power at 0.25 Hz, which is typically higher than normal for
345 hemodynamics, could be a result of increased vasomotion. Evidence from prior work in human
346 laser doppler flowmetry and magnetoencephalography (MEG) has suggested that stroke affected
347 arterioles showed elevated power^{41,42}.

348 We then asked if this increase in power of the GCaMP, in the contralesional hemisphere,
349 and hemodynamic signal, in both hemispheres, was uniform across the hemispheres or specific to
350 any distinct brain region. Fig 4e shows spatial maps of the average power for GCaMP and HbO
351 for one typical mouse. We clearly see increased power in GCaMP in the contralesional hemisphere
352 and increased overall power in HbO at day2 and week 1 compared to pre-stroke. Surprisingly, the
353 increase in GCaMP power appeared specific to the contralesional forelimb region, while the power
354 increase in HbO appeared global. This was validated across all mice (Fig 4f), which showed that
355 there was a significant increase in power within only the contralesional forelimb and not the rest

356 of the contralesional hemisphere. The HbO signal on the other hand showed increases across all
357 regions, the ipsilesional and contralesional forelimb and non-forelimb areas. There was also a
358 decrease in the GCaMP signal within the ipsilesional forelimb region in the chronic phase, which
359 is likely due to loss of neurons within that region.



361 **Figure 4: Global brain oscillations following stroke.** (a) Raw time traces of filtered (0.009-0.4
362 Hz) calcium and hemodynamic signals before and 2 days after stroke within the ipsilesional (top)
363 and contralesional (bottom) hemispheres in ROI marked with pink box. Note the increase in
364 amplitude of HbO in both hemispheres at day 2 and increase in GCaMP amplitude only in the
365 contralesional hemisphere. (b) Histogram of variance in the mean signal, after global signal
366 regression, for GCaMP (left) and HbO (right) at pre-stroke, day 2, and week 4. (c) Frequency
367 spectrum of the power of the GCaMP (left) and HbO (right) signal in the ipsilesional (top) and
368 contralesional (bottom) hemispheres. (d) Area under the curve within 0.1-0.3 Hz frequency band.
369 Thick bars: $p < 0.01$, thin bars: $p < 0.05$. (e) Spatial maps of average power across 0.009-0.4 Hz
370 frequency band for GCaMP (top) and HbO (bottom) at each time point. (f) Mean power assessed
371 in each hemisphere within the forelimb and non-forelimb areas. Thick bars: $p < 0.01$, thin bars:
372 $p < 0.05$.

373

374 **Photothrombotic stroke disrupts resting state interhemispheric functional connectivity only
375 in the very acute phase**

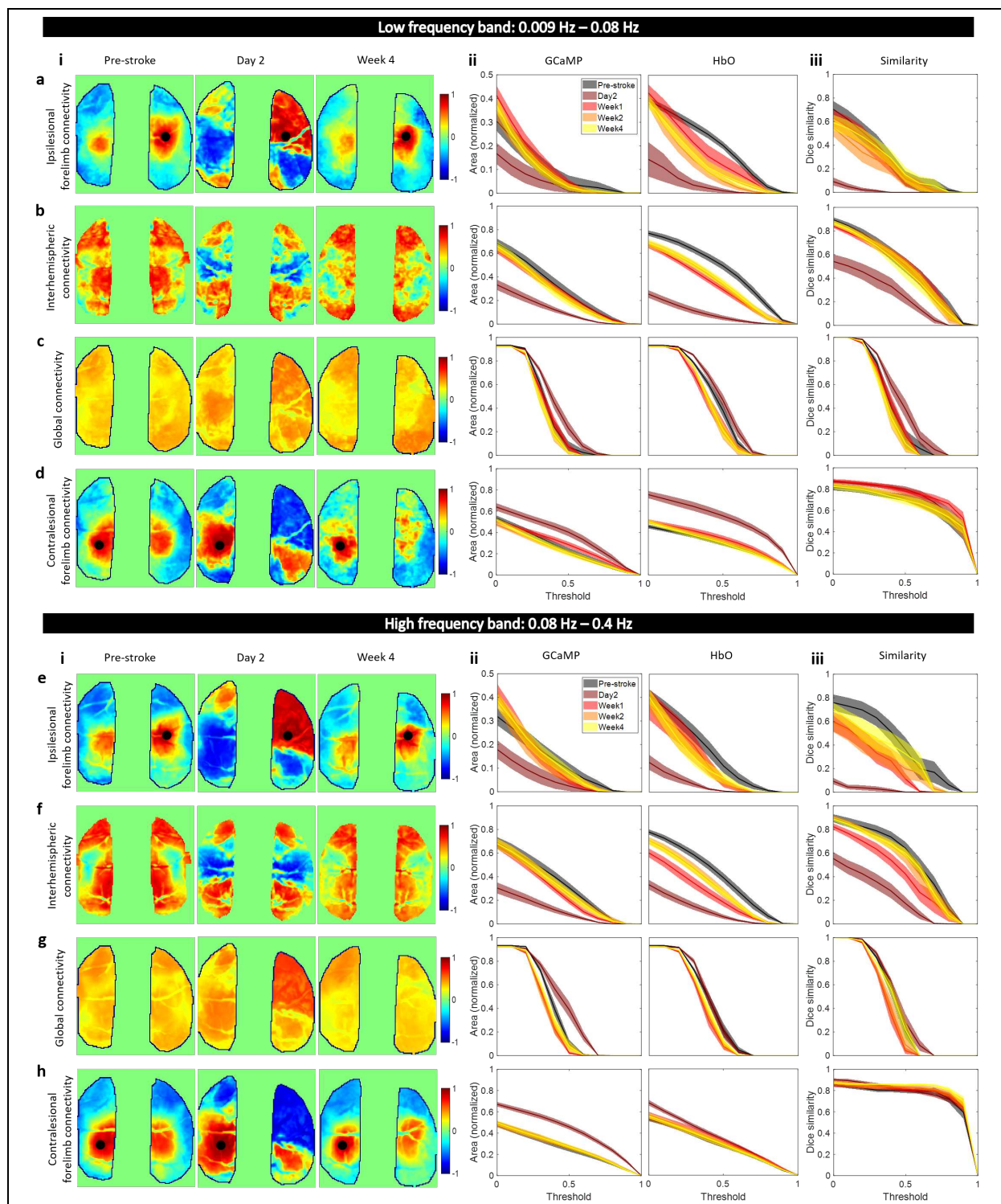
376 Stroke has also been known to affect functional connectivity across large scale brain networks^{43,44}.
377 To address the possibly differential effects of stroke on calcium and hemodynamic global brain
378 dynamics we asked whether resting state functional connectivity (RSFC) showed similar dynamics
379 during the recovery phase. Prior work in healthy animals has showed that at low (0.009-0.08 Hz)
380 and high (0.08-0.4 Hz) frequency bands, which are typically used in BOLD fMRI and functional
381 connectivity IOSI studies, functional connectivity structures between GCaMP and HbO were in
382 high agreement³³. But as applications of hemodynamic RSFC are extended into the stroke field it
383 is not only important to understand the underlying physiology that those signals represent but also
384 what aspects of connectivity are altered and are sensitive measures for the stroke^{29,45}.

385 To that end, we looked at various aspects of RSFC in the low and high frequency bands
386 across the GCaMP and HbO maps. First, we assessed connectivity of the ipsilesional forelimb area
387 to the contralesional hemisphere (Fig 5a). In healthy pre-stroke animals, seed-based forelimb
388 connectivity maps were consistently normal when compared to prior work, while acute stroke

389 showed alterations in forelimb connectivity to the contralesional hemisphere⁴⁵⁻⁴⁷. Fig 5a(i) shows
390 the forelimb connectivity maps for GCaMP at pre-stroke, day2, and week4 in the low frequency
391 band. We then quantified the differences between pre-stroke and each post-stroke time point by
392 calculating the proportional area of the cortex above a certain correlation coefficient threshold that
393 ranged from 0 to 0.9 (Fig 5a(ii)). A slight decrease in connectivity was observed in the GCaMP
394 map and a large decrease was observed in HbO at 2 days post-stroke (Fig 5a(ii), Supplementary
395 Fig 8a). HbO continued to show reduced forelimb connectivity at all time points after stroke at
396 specific thresholds (Supplementary Fig 8a), however, GCaMP connectivity appeared largely
397 restored at later time points. A Dice similarity index was calculated between the GCaMP and HbO
398 maps across all thresholds, which showed a deviation in similarity only at day2 after stroke, while
399 maps were consistent at all other time points (Fig 5a(iii), Supplementary Fig 5a). A similar
400 approach was used for calculating interhemispheric connectivity, global connectivity, and
401 contralesional forelimb intrahemispheric connectivity as well as all measures in the higher
402 frequency band. Trends across time points and thresholds for all measures were largely similar in
403 both frequency bands. There was a significant drop in interhemispheric connectivity at 2 days in
404 both GCaMP and HbO, which was restored at later time points in GCaMP but continued to persist,
405 to a lesser extent, in HbO until week1 (Fig 5b,f). Surprisingly there was a small but significant
406 increase in global connectivity at day2 in GCaMP (Fig 5c,g, Supplementary Fig 8c). Spontaneous
407 recovery over four weeks resulted in reestablishment of global connectivity networks in both
408 GCaMP and HbO. Since we observed increase in the calcium power within the contralesional
409 hemisphere (previous section) we also asked whether contralesional forelimb connectivity was
410 altered. We observed a significant increase in contralesional forelimb connectivity within the
411 contralesional hemisphere at day 2 after stroke (Fig 5d,e). This suggests that increases in the power

412 of the calcium signal within the contralesional forelimb was associated with an increase in its
413 functional connectivity to other regions of the brain. The increase observed in the global
414 connectivity index could be due to this increased connectivity of the contralesional forelimb.

415 From these data we extrapolate that connectivity of both the impaired and unimpaired
416 forelimb and interhemispheric connectivity for both GCaMP and HbO were reliable measures to
417 indicate stroke, given our photothrombotic model, at day 2. Disruptions to interhemispheric
418 connectivity persisted until week 1 after stroke, however other metrics assessed were
419 indistinguishable from pre-stroke. While global connectivity provides a concise method as a seed-
420 independent approach of functional connectivity, in our case it was a weaker metric for following
421 the stroke recovery process.



422

423 **Figure 5: Global brain network dynamics assessed with RSFC.** Spatial maps of ipsilesional
424 forelimb connectivity (a(i),e(i)), interhemispheric connectivity (b(i),f(i)), global connectivity
425 (c(i),g(i)), and contralateral forelimb connectivity (d,h) at pre-stroke, day 2, and week 4. Proportional area of cortex over
426 threshold for GCaMP and HbO at each time point for ipsilesional forelimb connectivity (a(ii),e(ii)),
427

428 interhemispheric connectivity (b(ii),f(ii)), global connectivity (c(ii),g(ii)), and contralesional
429 forelimb connectivity (d(ii),h(ii)) in the low frequency band (a,b,c,d) and in the high frequency
430 band (e,f,g,h). Dice similarity coefficient for overlap between area covered by GCaMP and HbO
431 for ipsilesional forelimb connectivity (a(iii),e(iii)), interhemispheric connectivity (b(iii),f(iii)),
432 global connectivity (c(iii),g(iii)), and contralesional forelimb connectivity (d(iii),h(iii)) at all time
433 points in the low frequency band (a,b,c,d) and the high frequency band (a,b,c,d).

434

435 **Correlating acute phase cortical metrics to long-term behavior outcomes**

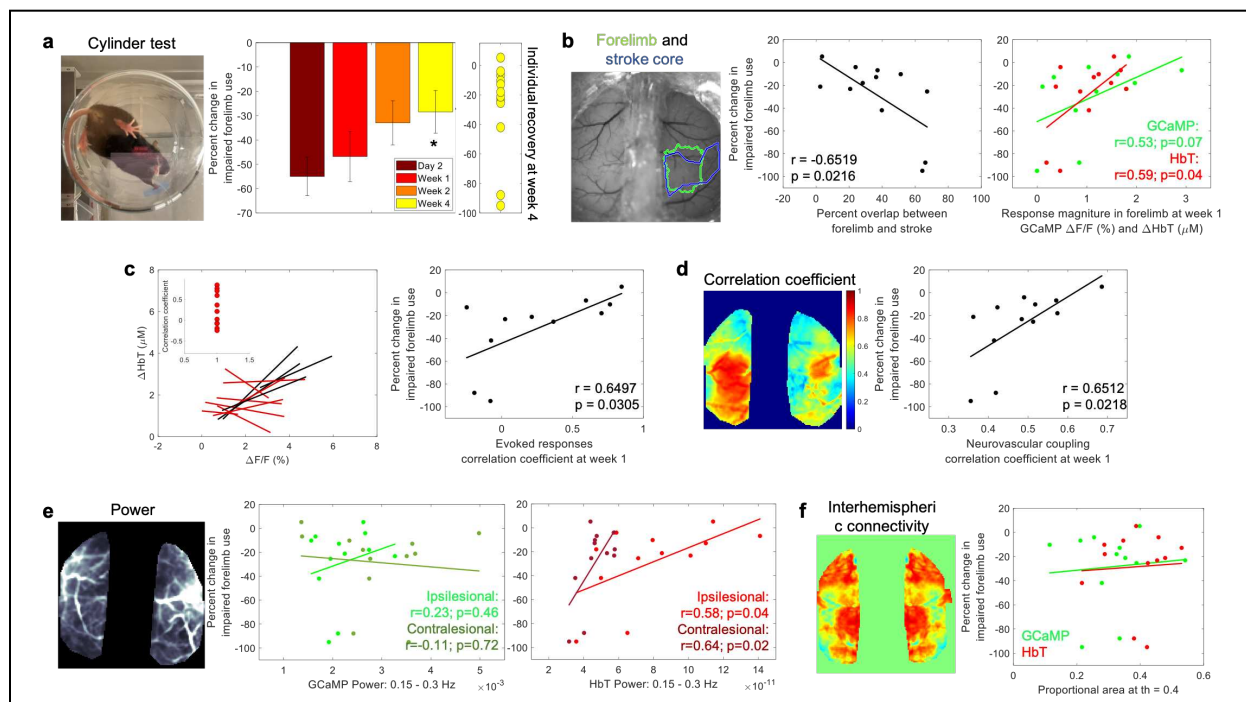
436 To enable translation of the cortical measures investigated in this work to potentially clinically
437 relevant outcomes, we measured forelimb performance through the cylinder asymmetry test before
438 stroke and at each imaging time point after stroke. Photothrombotic stroke to the forelimb
439 somatosensory area led to deficits in the use of the impaired forelimb (Fig 6a). Mice used their
440 impaired forelimb 50% less than baseline in the first week following stroke, however, over time
441 with spontaneous recovery, mice showed a significant increase in the use of the impaired forelimb
442 by week 4 compared to day 2 (Fig 6a). An important factor in human strokes that is often missed
443 in animal models is the variability in the extent of damage and impairment caused by the stroke.
444 The extent and location of the damage due to stroke as well as the early spontaneous recovery
445 mechanisms play a significant role long-term outcome^{3,4,48}. A number of early biomarkers that
446 might have potential as indicators of behavioral outcome are under active investigation in both
447 humans and in animal studies^{49,50}. While it would be ideal to introduce a controlled level of
448 variability into animal models to study variable recovery and to identify biomarkers that indicate
449 recovery, such a method of stroke induction does not yet exist that also meets all the other criteria
450 for a physiological stroke, such as preventing the use of anesthesia during stroke induction. Our
451 optimized photothrombotic model introduces uncontrolled variability that mimics human
452 variability to some extent and allows correlation of behavioral outcome to cortical biomarkers.
453 The right panel of Fig 6a shows the extent of recovery in forelimb asymmetry for individual mice

454 at week 4. In this section we outline how cortical measures obtained in all the previous sections
455 correlate to these variable long-term behavioral outcomes.

456 First, since the cylinder test is sensitive to forelimb use, we tested whether the extent of
457 forelimb area that was damaged due to stroke predicted behavioral outcomes. We calculated the
458 percent overlap between the pre-stroke forelimb region and the stroke outline obtained at 1 week
459 after stroke from SFDI (Fig 6b). There was a significant negative correlation indicating that worse
460 behavior outcomes correlated with a larger portion of the forelimb being damaged by the stroke.
461 We next asked whether functionality in the surviving portion of the forelimb region promoted
462 behavioral recovery. Here, we calculated the magnitude of responses within the original forelimb
463 region for GCaMP and hemodynamics at week 1. Both GCaMP and hemodynamics showed trends
464 towards a positive correlation between response magnitude and better outcomes, with only the
465 HbT showing a significant correlation (Fig 6b). Next, we assessed the relationship between acute
466 neurovascular coupling and behavior outcomes. This was calculated in two ways, using the
467 correlation between GCaMP and HbT responses and using HRF. The correlation coefficients
468 obtained from the magnitude of evoked responses between GCaMP and HbT at week 1 during
469 forelimb stimulation significantly correlated with behavioral outcomes (Fig 6c, data from Fig 2).
470 The correlation coefficients obtained from the neurovascular coupling HRF model between the
471 measured and estimated HbT at week 1 also showed a significant correlation with behavioral
472 outcomes implying that preserved or improved neurovascular coupling at week 1 might be
473 indicative of better long-term recovery (Fig 6d).

474 We performed similar calculations with the global brain metrics of power of the signal and
475 interhemispheric connectivity from RSFC. Average power was calculated within the narrow
476 frequency band (0.15–0.3Hz) for both GCaMP and hemodynamics and separated into ipsilesional

477 and contralesional hemispheres. While GCaMP did not show any trends with behavior, acute
478 hemodynamic oscillations showed strong positive trends with behavior outcomes (Fig 6e).
479 Specifically, increased power in the HbT signal of the contralesional and ipsilesional hemispheres
480 in the acute phase of stroke significantly correlated with behavior outcomes. Interhemispheric
481 connectivity at week 1, or any other RSFC metric, did not show any correlations with long-term
482 behavior outcomes, further implying that RSFC might not be a sensitive metric for targeted
483 photothrombosis. Overall, we have identified several cortical metrics within the acute phase of
484 stroke recovery that had the potential to delineate animals that tend to show better spontaneous
485 recovery versus animals that had poorer recovery.



486
487 **Figure 6: Correlating cortical metrics to behavior outcomes.** (a) Forelimb asymmetry, assessed
488 with the cylinder test, calculated as a change in impaired forelimb use from pre-stroke, right:
489 recovery of individual mice at week 4. (b) Left: reference image showing outlines of pre-stroke
490 forelimb region and stroke core at 1 week, middle: correlation between overlap of forelimb and
491 stroke with forelimb asymmetry at week 4, right: correlation between response magnitude at week
492 1 for GCaMP and HbT with forelimb asymmetry at week 4. (c) Left: correlation of evoked
493 responses of GCaMP and HbT, right: correlation between the correlation coefficient of evoked
494 responses at week 1 and forelimb asymmetry at week 4. (d) Left: correlation coefficient between
interhemispheric connectivity at week 1 and forelimb asymmetry at week 4, right: correlation between
neurovascular coupling at week 1 and forelimb asymmetry at week 4. (e) Left: power spectra of
GCaMP and HbT, right: correlation between power spectra and forelimb asymmetry. (f) Left:
interhemispheric connectivity, right: correlation between GCaMP and HbT with forelimb asymmetry at
week 4.

495 measured HbT and HbT predicted by convolving GCaMP and IRF, right: correlation between
496 neurovascular coupling correlation coefficient at week 1 and forelimb asymmetry at week 4. (e)
497 Correlation between power of GCaMP and HbT in frequency band 0.15-0.3 Hz in the ipsilesional
498 and contralesional hemispheres and forelimb asymmetry at week 4. (f) Correlation between resting
499 state interhemispheric connectivity and forelimb asymmetry at week 4.

500

501 **Discussion**

502 While functional neuroimaging has great potential for treating and monitoring patients in the acute
503 and chronic phases of stroke recovery, the interpretations of these signals and their reliability as a
504 neural correlate is still under active investigation. In this study, we used an animal model of stroke,
505 which was optimized for high clinical relevance, to investigate the relationships between neural
506 activity, assessed with a fluorescent calcium indicator, and cerebral blood volume, assessed with
507 changes in oxy and deoxy hemoglobin, during longitudinal stroke recovery. We showed that acute
508 stroke leads to disruptions in neurovascular coupling, which is restored in the chronic phase.
509 Neurovascular uncoupling was primarily experienced within the affected hemisphere and early
510 recoupling and recovery of cortical function within the preserved forelimb region and peri-infarct
511 zone was an indicator of better recovery. Additionally, we showed that acute stroke leads to
512 increases in global brain oscillations, which show distinct spatial characteristics in GCaMP and
513 hemodynamics.

514 The results from this study have several implications for the interpretations of
515 hemodynamic signals in terms of the underlying physiology in both pre- and post-stroke. In the
516 healthy brain we showed that with simultaneous multi-modal imaging of neural calcium activity
517 and hemodynamics we can track subtle differences in sensory evoked response dynamics on a
518 trial-by-trial basis. This allowed us to correlate intra-animal changes to evoked responses across
519 the cohort and at each time point after stroke. We correlated each animal's responses individually

520 due to the variability in the extent of ischemic damage among animals introduced by our stroke
521 model. This allowed us to track the changes in each animal individually and we found that there
522 was a significant loss in correlation between evoked calcium and hemodynamic responses in the
523 acute phase at day 2 and week 1. Correlation was reestablished in most animals by week 4
524 signifying spontaneous recovery and improved behavior. A small number of animals continued to
525 show loss of correlation between evoked calcium and hemodynamic responses across both the
526 acute and chronic time points and these animals were associated with poor behavior outcomes.
527 There was also a significant positive trend between correlation of evoked responses, specifically
528 between calcium and HbT, at week 1 and behavior outcomes at week 4 across all mice. Taken
529 together with the significant correlation between early HbT response magnitudes within preserved
530 forelimb and long-term behavior, this implies that early recovery of hemodynamic responses, HbT
531 in particular, might be indicative of better outcomes.

532 While correlations of evoked calcium and hemodynamic response magnitudes allowed us
533 to draw conclusions about the similarity, or dissimilarity in the case of stroke, between the two
534 measures, it does not contain quantitative information about their relationship. To quantitatively
535 describe neurovascular coupling, we predicted hemodynamics from calcium activity using linear
536 least-squares deconvolution as had been done previously^{32,38}. Similar to previous reports, the
537 measured calcium signal convolved with a calculated HRF kernel predicted the hemodynamic
538 signal to a high degree in healthy animals. There was a higher correlation within sensory regions
539 of both hemispheres compared to more frontal or posterior regions, likely due to sensory
540 stimulation driving cortical activity within somatosensory cortex and strengthening the observed
541 neurovascular coupling signal. The characteristic shape of the HRF was altered after acute stroke,
542 which also corresponded with a significant decrease in the ability of the model to predict

543 hemodynamics within the affected hemisphere. The correlation when using the pre-stroke
544 “healthy” HRF was significantly lower than the correlation when using the time-point specific
545 post-stroke HRF. This indicates that while the model post-stroke was finding the best fit, the
546 resulting HRF was not necessarily similar to the expected neurovascular coupling model under
547 healthy conditions. Using the expected neurovascular coupling model yielded significantly worse
548 correlations. These results suggest that the neurovascular coupling model established in healthy
549 animals was not representative of post-stroke acute phase dynamics and that the observed
550 hemodynamic response is not an accurate representation of the underlying physiology since the
551 HRF was unable to predict hemodynamics accurately during the acute phase. However, it must
552 also be noted that the model assumption of a linear relationship might not hold true after stroke,
553 and the hemodynamic response might be better predicted with an altered non-linear model.
554 Nevertheless, we see restoration of neurovascular coupling, in accordance with the linear model,
555 in the chronic phase of recovery. We observed reestablishment of the expected HRF shape and
556 improvement in the ability of the model to predict hemodynamics, specifically in the peri-infarct
557 region. This suggests that functional neuroimaging might be faithfully representing the underlying
558 neurophysiology in the chronic phase.

559 In addition to local changes to evoked responses and neurovascular coupling alterations
560 within the affected hemisphere, stroke is known to have a profound impact on global cortical
561 network dynamics such as contralateral and subcortical connectivity⁴⁴. We found that there was
562 an increase in the overall power of cortical signals in both calcium and HbT in the acute phase,
563 which was resolved in the chronic phase. The increase in power of the calcium signal appeared to
564 be specific to the contralateral forelimb region, while the increase in hemodynamic power was
565 global across all vessels and both hemispheres. A prior study conducted with laser doppler

566 flowmetry showed increased oscillations within stroke affected arterioles and suggested increased
567 vasomotion as the cause⁴². Other studies have also showed increases in brain oscillations in stroke
568 and traumatic brain injury^{41,51,52}. Vasomotion, which is the oscillating tone of blood vessels
569 independent of heart rate or breathing, is tightly regulated, and maintained by various
570 compartments of the neurovascular unit^{53,54}. Vascular autoregulation is impaired after stroke and
571 ionic imbalances in neural, astroglial, and endothelial cells could result in dysregulation of
572 vasoactive molecules and ions and therefore vascular tone^{17,18}. On the other hand, we also observed
573 increases in power of GCaMP in the contralesional forelimb. Prior work has shown that stroke
574 leads to increases in brain excitability and disruption of the interhemispheric inhibition through
575 the corpus callosum^{55–57}. This could reduce the inhibitory effects that the two hemispheres exert
576 on each other, which could increase excitability within the contralesional hemisphere. There is
577 also evidence of thalamic disinhibition within minutes of ischemic stroke that can unmask
578 ipsilateral pathways⁵⁸. The excitability of thalamocortical pathways contralateral to the stroke may
579 be enhanced because of downregulation on interhemispheric thalamic inhibition. Surprisingly, we
580 found that increased power in the hemodynamic signal in the contralesional hemisphere during the
581 acute phase was correlated with improved behavior outcomes. Prior work has shown that
582 stimulation of activity within the gamma frequency band improved cerebral blood flow, decreased
583 infarct volume, and improved motor behavior, suggesting that modulation of cortical oscillatory
584 dynamics may serve as a target for neuroprotection⁵⁹. Other studies have also shown that increased
585 brain oscillations and excitability promoted recovery in stroke as well as other neurological
586 disorders and suggest its possible use as a biomarker for recovery^{51,55,56,60}. A meta-analysis on
587 activation data from over 50 neuroimaging experiments have shown enhanced activity in the
588 homotopic region of the contralesional hemisphere in the acute phase after stroke^{61,62}. This

589 enhanced activity appears as spontaneous and synchronous neural activity and has been shown to
590 be a signal for axonal sprouting and reorganization⁶³. Taken together with this evidence, we could
591 hypothesize that spontaneous increases in power that we observed in hemodynamic activity might
592 play a role in promoting recovery mechanisms. These oscillations are possibly driven by
593 underlying neural activity at frequencies higher than we can measure with GCaMP, which we are
594 unable to capture due to the slow calcium dynamics compared to neural firing.

595 A growing number of studies are now using RSFC to assess spatiotemporal correlations in
596 spontaneous hemodynamic signals across different brain regions in healthy and diseased states. In
597 the healthy brain, hemodynamic signals have been found to be bilaterally correlated and
598 synchronized temporally in functionally distinct brain regions and represent the connectivity of
599 underlying intrinsic neural fluctuations^{32,46,64}. RSFC has also been used as a sensitive assay to
600 monitor progression of stroke and hemorrhage with the assumption that the altered connectivity
601 represents the altered neural state^{29,45}. In this study we show that RSFC of spontaneous calcium
602 activity and hemodynamics show similar trends after stroke, validating prior assumptions.
603 Forelimb and interhemispheric connectivity were disrupted significantly in the very early acute
604 phase and was resolved within week 1 in both calcium and hemodynamics. Moreover, we found
605 that RSFC measures were not predictive of behavioral outcome. This could be because global brain
606 connectivity is more robust to small strokes caused by targeted photothrombosis to the forelimb.
607 A prior RSFC study also showed that somatosensory connectivity was not predictive of behavior
608 but motor and retrosplenial cortices might be better predictors²⁹. Due to our window preparation
609 procedure and headbar design for multimodal optical access we were limited in the field-of-view
610 to mainly the somatosensory region and were unable to capture connectivity to other brain regions
611 to their full extent. It is also possible that more sensitive analyses are needed for RSFC to serve as

612 a metric for stroke outcome. We also tested whether increases in power of the calcium activity
613 within the contralesional forepaw was associated with increased functional connectivity through
614 RSFC. We found that intra-contralesional hemisphere connectivity was significantly increased at
615 day 2. This suggests that increased excitability within the contralesional forepaw might result in
616 its increased functional connectivity to surrounding regions as well as the ipsilesional peri-infarct,
617 as seen from the spatial maps of connectivity. Further investigation is needed to understand the
618 link between excitability and functional connectivity and its impact on recovery.

619 An important factor to note in our study is that we measure calcium dynamics from only
620 excitatory cells. We know, from decades of prior work, that both excitatory and inhibitory cells
621 have important and distinct roles to play in maintaining cortical balance⁶⁵. Additionally, a number
622 of other cell types, such as astrocytes and pericytes, and modulators are involved in regulating
623 blood flow to meet the metabolic demands of the brain^{14,66,67}. We also know that these different
624 cell types are impacted differently after stroke^{1,2,68}. While the current study used mice with labelled
625 excitatory neurons, the same imaging platform and experimental design can be used to investigate
626 the contributions of other cell types, such as inhibitory cells and glia, to alterations in neurovascular
627 coupling after stroke. Additionally, calcium dynamics assessed with GCaMP6f has been validated
628 to be a reliable measure of neural activity, however, it is still not a direct measure of neural
629 electrical activity. Fast neural dynamics or sub-threshold dynamics may be missed in calcium
630 imaging since the dynamics of calcium are much slower than action potentials or local field
631 potentials. Although performing similar experiments while capturing local field potentials would
632 allow us to assess neural activity directly and provide a higher temporal resolution, we do not
633 believe that using GCaMP has affected our assessment of neurovascular coupling as all our

634 experiments are performed at a temporal resolution higher than what is needed for hemodynamics
635 assessment.

636 In summary, by simultaneously capturing changes in neural calcium activity and
637 hemodynamics we have assessed various aspects of neurovascular coupling during the acute and
638 chronic phases of stroke recovery. Our data suggest that acute stroke leads to neurovascular
639 uncoupling, implying that functional neuroimaging by fMRI and fNIRS might not accurately
640 represent the underlying neural activity and one needs to use caution when interpreting the results.
641 Neurovascular coupling is restored in the chronic phase, suggesting that these functional
642 neuroimaging methods more faithfully represent the underlying neural activity chronically.
643 Moreover, early recovery of neurovascular coupling and increased power of brain oscillations were
644 predictors of better long-term behavioral outcomes.

645

646

647

648

649

650

651

652

653

654 **Methods**

655

656 **Experimental design**

657 All experiments and animal procedures were approved by the Boston University Institutional
658 Animal Care and Use Committee and were conducted following the Guide for the Care and Use
659 of Laboratory Animals. All animals used in this study were adult Thy1-GCaMP6f mice (Jackson
660 Labs, strain code: 025393, C57BL/6J-Tg(Thy1-GCaMP6f)GP5.17Dkim/J)). The mice were
661 implanted with bilateral cranial windows, one window on each of the hemispheres, and allowed to
662 recover for two weeks. Following recovery, mice underwent a habituation training in a custom
663 imaging cradle to get accustomed to the imaging setup and environment. Pre-stroke control
664 measures were obtained one week prior to stroke and photothrombotic stroke was performed on
665 Day0 of the experiment. Following photothrombosis, mice were imaged longitudinally at Day2,
666 Week1, Week2, and Week4 to span both the acute and chronic phases of stroke recovery. To
667 correlate the cortical measures to a behavior metric, forelimb asymmetry was measured using the
668 cylinder test at each of the imaging time points. The timeline of experiments is outlined in Fig. 1a.

669

670 **Animal preparation**

671 A bilateral cranial window exposing both hemispheres of the brain was implanted in all mice to
672 determine the effect of stroke on both the ipsilesional and contralateral hemispheres. The surgical
673 procedure for implantation of bilateral cranial windows followed a similar procedure to unilateral
674 windows that has been previously described⁶⁹. Briefly, mice were injected with Buprenorphine
675 subcutaneously 1 hour prior to the start of surgery. During surgery, mice were anesthetized with

676 isoflurane (3% at induction and 1-1.5% for maintenance with 1L/min oxygen) and body
677 temperature was maintained at 37°C. Respiratory rate and toe pinch were used to monitor the depth
678 of anesthesia throughout the surgical procedure. After incision of the scalp, a round aluminum
679 head post, 12mm in diameter, was attached to the intact skull with dental acrylic. A craniotomy
680 was performed on one hemisphere of the brain in order to remove the skull. A half-skull-shaped
681 curved glass (modified from Crystal Skull⁷⁰, LabMaker, Germany) was used to cover the surface
682 of the brain and then sealed with optical glue and dental acrylic. The craniotomy and glass
683 procedure were repeated on the other hemisphere of the brain in order to create a bilateral cranial
684 window implant. Recovery procedures were followed according to the guidelines provided by
685 Boston University. After a two-week recovery period from surgery, mice were trained to remain
686 head-fixed for up to 90 min for approximately 10 days. All experiments are done in awake head-
687 fixed mice.

688

689 **Simultaneous hemodynamic and calcium imaging**

690 To evaluate local and global changes in neurovascular coupling post-stroke simultaneous measures
691 of hemodynamic and neural activity were obtained during forelimb sensory stimulation and resting
692 state. The instrumentation, task setup, and data analysis pipeline for measuring cortical
693 hemodynamics has been outlined previously⁶⁹. Fig. 1a shows a simplified schematic of the imaging
694 setup. Intrinsic optical signal imaging was used to assess changes to oxy and deoxy hemoglobin,
695 HbO and HbR respectively, for the hemodynamic measure, and fluorescence GCaMP imaging was
696 performed to assess changes in calcium dynamics as a measure of neural activity. The cortical
697 windows were illuminated sequentially with 470 nm, 530 nm, and 625 nm LEDs (MXL3-C1,
698 Thorlabs, X is the center wavelength), where the 470 nm LED was used for GCaMP excitation

699 and the 530 nm and 625 nm LEDs were used for calculations of oxy and deoxy hemoglobin. A
700 500 nm long pass filter (FELH0500, Thorlabs) placed along the detection path blocked out any
701 GCaMP excitation light. Images were collected by a sCMOS camera (Hamamatsu ORCA-Flash
702 4.0 V3) at 15 Hz, 5 Hz per wavelength, with an exposure time of 50 msec. For resting state,
703 spontaneous activity was obtained for 8 min. For sensory stimulation, two imaging session were
704 performed at each time point pre- and post-stroke, one where the contralateral (affected) forelimb
705 was stimulated and the second where the ipsilateral (unaffected) forelimb was stimulated. Each
706 stimulation session consisted of 20 trials where each trial was obtained in a block-design fashion
707 and consisted of 5 seconds of baseline, followed by 5 seconds of 3Hz air-puff stimulation, followed
708 by 20 seconds of recovery. A custom MATLAB code was used to synchronize and trigger the
709 sequential LEDs, camera acquisition, and air puff stimulation. Raw images at 530 nm and 625 nm
710 were analyzed for changes in oxy- and deoxy- hemoglobin using the modified Beer-Lambert
711 relationship as described previously^{69,71}. Calcium dynamics were analyzed as a change in
712 fluorescence over time from the interspersed raw images excited at 470 nm. The fluorescence data
713 were corrected for hemodynamic crosstalk as hemodynamic changes contaminate the fluorescence
714 signal and both the excitation and emission wavelengths. The correction algorithm used has been
715 previously described and modified from Ma et al³². The correction implemented estimates the
716 attenuation experienced by the GCaMP signal from the simultaneously obtained changes in oxy
717 and deoxy hemoglobin concentration. The change in calcium concentration is approximately equal
718 to the change in GCaMP fluorescence scaled by a time-varying hemoglobin absorption factor at
719 both the GCaMP excitation and emission wavelengths. The pathlength factor used for correction
720 is obtained from Monte Carlo simulations of photon transport using the Monte Carlo eXtreme
721 (MCX) platform^{72,73}. The absorption and scattering coefficients used for the MCX simulation were

722 obtained from spatial frequency domain imaging (described below). For pre-stroke imaging, a
723 single absorption and scattering coefficient, yielding a single pathlength, was used for correction
724 of all pixels. After stroke, the absorption and scattering coefficients used were determined on a
725 semi pixel-by-pixel basis. This modified correction technique was introduced in order to account
726 for changes in tissue optical properties after stroke^{74,75}. A Monte Carlo simulation was run on any
727 pixel that had a scattering coefficient that was 30% larger than the mean scattering coefficient of
728 the control animals, using the respective absorption and scattering coefficients of that pixel. This
729 new pathlength was used for the correction of pixels within the stroke region that had increased
730 scattering. The attenuation correction applied spatial maps and temporal traces are shown in Fig.
731 1b.

732

733 **Spatial frequency domain imaging**

734 To capture the spatial extent of the stroke core longitudinally as well as to aid in fluorescence
735 correction for hemodynamic crosstalk, SFDI was performed pre-stroke and at each time point post-
736 stroke. The instrumentation, acquisition, and analysis to obtain absorption and scattering
737 coefficients of the tissue have been described previously⁷⁴. Spatially varying sinusoidal patterns
738 were projected onto the cranial window by a digital micromirror device (DMD), and the reflected
739 light was imaged by the sCMOS camera. Two spatial frequencies (0 and 0.4 mm⁻¹) were projected
740 at three phases (0, 120, and 240 deg). The acquired images were processed offline using
741 MATLAB. The intensity at each spatial frequency was demodulated and calibrated to a reference
742 phantom to obtain the diffuse reflectance. A two-frequency lookup table was generated by Monte
743 Carlo simulations at the two frequencies used for imaging from which absorption and scattering
744 coefficients were extracted. To obtain the spatial extent of the stroke core, the relative change in

745 scattering coefficient post-stroke was calculated with respect to pre-stroke scattering, and a semi-
746 automatic contour was applied using a custom MATLAB code, to create a stroke core outline. This
747 core outline was used as the boundary for the start of the peri-infarct zone⁷⁴. The peri-infarct zone
748 was defined as the region that extended 0.5mm outward from the stroke core outline. SFDI was
749 also used in the correction of GCaMP for hemodynamic crosstalk. The absorption and scattering
750 properties obtained at each time point post-stroke were used to run the Monte Carlo simulation to
751 determine the pathlength of light travelled in tissue. This pathlength is then used in the correction
752 algorithm to scale the GCaMP signal, based on the time-varying changes in hemodynamic
753 absorption, for accurate estimation of calcium dynamics.

754

755 **Resting state functional connectivity analysis**

756 Global network connectivity changes following stroke were assessed using resting state functional
757 connectivity as described previously by a number of groups^{40,45,47}. Time traces of HbO and
758 GCaMP were bandpass filtered into two frequency bands, the typically used infraslow (0.008-0.09
759 Hz) frequency band and a higher frequency band (0.09-0.4 Hz) and regressed to remove any global
760 fluctuations in the signal. To evaluate the strength of network connections to the affected forelimb
761 region, a seed was placed in the center of the original forelimb somatosensory region of the
762 affected hemisphere. The seed time trace was calculated by averaging the time trace within 0.25
763 mm of the seed location and connectivity was assessed by calculating the correlation between the
764 seed time trace and the time course of every other pixel. By averaging the positive correlation
765 coefficients between the forelimb seed and all pixels that lie in the contralateral forelimb region
766 we calculated a forelimb connectivity map⁴⁷. Interhemispheric connectivity maps were calculated
767 by correlating each pixel within the affected hemisphere with its mirror pixel, mirrored along the

768 midline, in the unaffected hemisphere. The interhemispheric connectivity index was then
769 calculated by averaging all the pixels within the homotopic map of the affected hemisphere⁴⁷. To
770 assess the overall connectivity of the brain, global connectivity maps were generated by calculating
771 the correlation of each pixel with every other pixel and then assigning the average positive
772 correlation coefficient to that pixel. From the global connectivity maps, a global connectivity index
773 was calculated by taking the mean of the correlation coefficients for all pixels within the map⁴⁷.

774

775 **Neurovascular coupling**

776 To assess the relationship between neural activity and hemodynamics, neurovascular coupling was
777 modeled using linear least-squares deconvolution³². The cortical hemodynamic response is known
778 to be a linear convolution of the cortical neural activity and an impulse response function (IRF).
779 The impulse response function, also called the hemodynamic response function, is the
780 hemodynamic response to a neural stimulus. In a linear system, the convolution can be expressed
781 as $y = X * h$, and can be represented as:

$$782 \begin{bmatrix} y_1 \\ y_2 \\ \vdots \\ y_t \end{bmatrix} = \begin{bmatrix} x_1 & 0 & 0 & \dots & 0 \\ x_2 & x_1 & 0 & \dots & 0 \\ \vdots & \vdots & \vdots & \ddots & \vdots \\ x_t & x_{t-1} & x_{t-2} & \dots & x_n \end{bmatrix} \begin{bmatrix} h_1 \\ h_2 \\ \vdots \\ h_n \end{bmatrix},$$

783 where X is the input to the system, which is the corrected GCaMP fluorescence signal, and the
784 length n used is 15 sec (from -5 sec to 10 sec), y is the output of the system, which is the
785 hemodynamic signal, and h is the system's impulse function. A direct solution to the linear system
786 could result in an ill-conditioned matrix and therefore a regularization term is added and the
787 solution is obtained by minimizing the cost function and setting the derivative of the cost function
788 to zero, as described previously, and is given by:

789
$$h = (X^T X + \lambda I)^{-1} X^T y.$$

790 The regularization term λ was chosen to be 0.1 through all the analysis. The deconvolution was
791 performed on a pixel-by-pixel basis at each time point post-stroke.

792

793 **Targeted photothrombosis**

794 Focal cerebral ischemia was performed using an optimized photothrombosis method described
795 previously⁶⁹. A distal branch of the middle cerebral artery supplying the forelimb somatosensory
796 region, determined through pre-stroke forelimb stimulation, was targeted for occlusion. A 520nm
797 laser diode with axial and lateral parameters of 104 μm and 6 μm was tuned to a minimal post-
798 objective power of 0.6 mW. These parameters were designed to occlude only the target vessel and
799 prevent laser damage to the surrounding tissue, thus ensuring that the ischemia procedure was
800 physiological in nature. Real-time changes to cerebral blood flow (CBF) were monitored through
801 laser speckle contrast imaging (LSCI). Ten minutes of baseline CBF was obtained following which
802 the mouse was lightly anesthetized to inject Rose Bengal (100 μl , 15 mg/ml in saline)
803 retroorbitally. The mouse was then immediately taken off isoflurane and allowed to recover, which
804 was determined by a return of CBF to baseline and the mouse exhibiting natural behaviors such as
805 whisking. Following recovery the green laser was turned on until the target vessel was occluded,
806 as indicated by the target branch disappearing on LSCI. Once the target branch was occluded, the
807 laser power was reduced to 0.5 mW for an additional minute and then turned off. If at any point
808 the target branch started flowing again, the laser was turned back on until occlusion. Additionally,
809 as described previously, two collateral branches were also targeted to obtain a stable infarct. The
810 procedure was followed for 1 hour from the initiation of photothrombosis.

811 **Behavioral testing**

812 The cylinder test was used in all mice to assess behavioral deficit in forelimb use over the course
813 of 4 weeks following stroke. Two sessions of pre-stroke testing was obtained the week before
814 stroke induction to assess basal preference in forepaw use. Following photothrombotic stroke,
815 mice were tested at 2 days, 1 week, 2 weeks, and 4 weeks. Each testing session involved placing
816 a mouse in a clear glass cylinder and videotaping its natural behavior from below for 15 minutes.
817 Forelimb use was assessed by counting the number of times the mouse used each forelimb to make
818 first contact with the cylinder wall during rears. Asymmetry in forelimb use after stroke was
819 quantified as a percent change from baseline use of the contralateral (affected) forelimb. Change
820 from baseline was used to compensate for the fact that some mice have a preference for one paw
821 over the other even before a stroke.

822

823 **Data analysis and Statistics**

824 All data was analyzed offline using custom MATLAB codes. Image analysis for SFDI, calcium
825 fluorescence, and evoked and resting-state intrinsic optical signal imaging has been outlined in
826 previous sections. The dice similarity coefficient for area overlap in evoked responses and RSFC
827 is calculated using the matlab function dice.m. The dice coefficient is twice the ratio of the
828 intersection of two binary images and the sum of the number of elements in each image, given by:

$$829 \quad dice(A, B) = \frac{2 |A \cap B|}{|A| + |B|}$$

830 Goodness-of-fit correlation and significance for stimulus evoked response magnitudes of GCaMP
831 and hemodynamics were made using a linear fit. All statistical analyses were made using

832 MATLAB with *post hoc* comparisons using t-tests. A two sample students t-test was performed
833 for comparing data points with pre-stroke data (matlab function: ttest2).

834

835 **Data and code availability statement**

836 The datasets generated and/or analyzed during this study and corresponding code that support the
837 findings of this study are available from the corresponding author upon request.

838

839 **Disclosures**

840 The authors declare no potential conflicts of interest with respect to the research, authorship, and/or
841 publication of this article.

842

843 **Acknowledgments**

844 This work was supported by the National Institute of Health [R01-EB021018, R01-NS108472,
845 R01-MH111359].

846

847 **Author contributions**

848 Conceptualization: SS, KK, EE, DAB
849 Methodology: SS, JJ, SK, KK, EE, DAB
850 Investigation: SS, ShS
851 Visualization: SS, DAB
852 Supervision: DAB, AD, CA
853 Writing: SS, EE, CA, AD, DAB
854

855

856

857

858 **References**

- 859 1. Moskowitz, M. A., Lo, E. H. & Iadecola, C. The science of stroke: Mechanisms in search
860 of treatments. *Neuron* **67**, 181–198 (2010).
- 861 2. Lo, E. H., Moskowitz, M. A. & Jacobs, T. P. Exciting, radical, suicidal: How brain cells
862 die after stroke. *Stroke* **36**, 189–192 (2005).
- 863 3. Sharma, N. & Cohen, L. G. Recovery of motor function after stroke. *Dev. Psychobiol.* **54**,
864 254–262 (2012).
- 865 4. Cramer, S. C. Repairing the human brain after stroke: I. Mechanisms of spontaneous
866 recovery. *Ann. Neurol.* **63**, 272–287 (2008).
- 867 5. Cassidy, J. M. & Cramer, S. C. Spontaneous & Therapeutic-Induced Mechanisms of
868 Functional Recovery After Stroke. *Transl. Stroke Res.* **8**, 33–46 (2017).
- 869 6. Jones, T. A. Motor compensation and its effects on neural reorganization after stroke. *Nat.*
870 *Rev. Neurosci.* **18**, 267–280 (2017).
- 871 7. Moseley, M. Mri of stroke. *Imaging* **41**, 410–414 (2010).
- 872 8. Veldsman, M., Cumming, T. & Brodtmann, A. Beyond BOLD: Optimizing functional
873 imaging in stroke populations. *Hum. Brain Mapp.* **36**, 1620–1636 (2015).
- 874 9. Lake, E. M. R., Bazzigaluppi, P. & Stefanovic, B. Functional magnetic resonance imaging
875 in chronic ischaemic stroke. *Philos. Trans. R. Soc. B Biol. Sci.* **371**, 1–11 (2016).
- 876 10. Johansen-Berg, H. *et al.* Correlation between motor improvements and altered fMRI
877 activity after rehabilitative therapy. *Brain* **125**, 2731–2742 (2002).
- 878 11. Pineiro, R., Pendlebury, S., Johansen-Berg, H. & Matthews, P. M. Altered hemodynamic
879 responses in patients after subcortical stroke measured by functional MRI. *Stroke* **33**, 103–
880 109 (2002).
- 881 12. Carter, A. R. *et al.* Resting state inter-hemispheric fMRI connectivity predicts
882 performance after stroke. *Ann. Neurol.* **67**, NA-NA (2009).
- 883 13. Corbetta, M. Functional connectivity and neurological recovery. *Dev. Psychobiol.* **54**,
884 239–253 (2012).
- 885 14. Kleinfeld, D. *et al.* A guide to delineate the logic of neurovascular signaling in the brain.
886 *Front. Neuroenergetics* **3**, 1–9 (2011).
- 887 15. Buxton, R. B., Griffeth, V. E. M., Simon, A. B. & Moradi, F. Variability of the coupling
888 of blood flow and oxygen metabolism responses in the brain: A problem for interpreting
889 BOLD studies but potentially a new window on the underlying neural activity. *Front.*
890 *Neurosci.* **8**, 1–6 (2014).
- 891 16. Logothetis, N. K., Pauls, J., Augath, M., Trinath, T. & Oeltermann, A. Neurophysiological
892 investigation of the basis of the fMRI signal. *Nature* **412**, 150–157 (2001).
- 893 17. Kunz, A. & Iadecola, C. Cerebral vascular dysregulation in the ischemic brain. *Handb.*

894 *Clin. Neurol.* **92**, 283–305 (2009).

895 18. Girouard, H. & Iadecola, C. Neurovascular coupling in the normal brain and in
896 hypertension , stroke , and Alzheimer disease Regulation of the Cerebral Circulation
897 stroke , and Alzheimer disease. **100***21*, 328–335 (2012).

898 19. Weber, R. *et al.* Early prediction of functional recovery after experimental stroke:
899 Functional magnetic resonance imaging, electrophysiology, and behavioral testing in rats.
900 *J. Neurosci.* **28**, 1022–1029 (2008).

901 20. Shih, Y. Y. I. *et al.* Imaging neurovascular function and functional recovery after stroke in
902 the rat striatum using forepaw stimulation. *J. Cereb. Blood Flow Metab.* **34**, 1483–1492
903 (2014).

904 21. Carmichael, S. T. Rodent models of focal stroke: Size, mechanism, and purpose. *NeuroRX*
905 **2**, 396–409 (2005).

906 22. Bacigaluppi, M., Comi, G. & Hermann, D. M. Animal models of ischemic stroke. Part
907 two: modeling cerebral ischemia. *Open Neurol. J.* **4**, 34–38 (2010).

908 23. Sommer, C. J. Ischemic stroke: experimental models and reality. *Acta Neuropathol.* **133**,
909 245–261 (2017).

910 24. Winship, I. R. & Murphy, T. H. In Vivo Calcium Imaging Reveals Functional Rewiring of
911 Single Somatosensory Neurons after Stroke. *J. Neurosci.* **28**, 6592–6606 (2008).

912 25. Brown, C. E., Aminoltejari, K., Erb, H., Winship, I. R. & Murphy, T. H. In Vivo Voltage-
913 Sensitive Dye Imaging in Adult Mice Reveals That Somatosensory Maps Lost to Stroke
914 Are Replaced over Weeks by New Structural and Functional Circuits with Prolonged
915 Modes of Activation within Both the Peri-Infarct Zone and Distant Sites. *J. Neurosci.* **29**,
916 1719–1734 (2009).

917 26. Harrison, T. C., Silasi, G., Boyd, J. D. & Murphy, T. H. Displacement of sensory maps
918 and disorganization of motor cortex after targeted stroke in mice. *Stroke* **44**, 2300–2306
919 (2013).

920 27. Clarkson, A. N. *et al.* Multimodal examination of structural and functional remapping in
921 the mouse photothrombotic stroke model. *J. Cereb. Blood Flow Metab.* **33**, 716–723
922 (2013).

923 28. Lim, D. H., LeDue, J. M., Mohajerani, M. H. & Murphy, T. H. Optogenetic Mapping after
924 Stroke Reveals Network-Wide Scaling of Functional Connections and Heterogeneous
925 Recovery of the Peri-Infarct. *J. Neurosci.* **34**, 16455–16466 (2014).

926 29. Bauer, A. Q. *et al.* Optical imaging of disrupted functional connectivity following
927 ischemic stroke in mice. *Neuroimage* **99**, 388–401 (2014).

928 30. Park, C. H. *et al.* Longitudinal changes of resting-state functional connectivity during
929 motor recovery after stroke. *Stroke* **42**, 1357–1362 (2011).

930 31. Schrandt, C. J., Kazmi, S. S., Jones, T. A. & Dunn, A. K. Chronic Monitoring of Vascular
931 Progression after Ischemic Stroke Using Multiexposure Speckle Imaging and Two-Photon

932 Fluorescence Microscopy. *J. Cereb. Blood Flow Metab.* **35**, 933–942 (2015).

933 32. Ma, Y. *et al.* Resting-state hemodynamics are spatiotemporally coupled to synchronized
934 and symmetric neural activity in excitatory neurons. *Proc. Natl. Acad. Sci.* **113**, E8463–
935 E8471 (2016).

936 33. Wright, P. W. *et al.* Functional connectivity structure of cortical calcium dynamics in
937 anesthetized and awake mice. *PLoS One* **12**, 1–27 (2017).

938 34. Tian, L. *et al.* Imaging neural activity in worms, flies and mice with improved GCaMP
939 calcium indicators. *Nat. Methods* **6**, 875–881 (2009).

940 35. Dana, H. *et al.* Thy1-GCaMP6 transgenic mice for neuronal population imaging in vivo.
941 *PLoS One* **9**, (2014).

942 36. Ma, Y. *et al.* High-speed, wide-field optical mapping (WFOM) of neural activity and
943 brain haemodynamics: Considerations and novel approaches. *Under Rev.* **371**, 20150360
944 (2016).

945 37. Montgomery, M. K. *et al.* Glioma-Induced Alterations in Neuronal Activity and
946 Neurovascular Coupling during Disease Progression. *Cell Rep.* **31**, 107500 (2020).

947 38. Lake, E. M. R. *et al.* Simultaneous cortex-wide fluorescence Ca²⁺ imaging and whole-
948 brain fMRI. *Nat. Methods* **17**, 1262–1271 (2020).

949 39. Winder, A. T., Echagarruga, C., Zhang, Q. & Drew, P. J. Weak correlations between
950 hemodynamic signals and ongoing neural activity during the resting state. *Nat. Neurosci.*
951 **20**, 1761–1769 (2017).

952 40. Wright, P. W. *et al.* Functional connectivity structure of cortical calcium dynamics in
953 anesthetized and awake mice. *PLoS One* **12**, (2017).

954 41. Laaksonen, K. *et al.* Alterations in Spontaneous Brain Oscillations during Stroke
955 Recovery. *PLoS One* **8**, (2013).

956 42. Goltsov, A. *et al.* Bifurcation in blood oscillatory rhythms for patients with ischemic
957 stroke: A small scale clinical trial using laser Doppler flowmetry and computational
958 modeling of vasomotion. *Front. Physiol.* **8**, 1–11 (2017).

959 43. Grefkes, C. & Fink, G. R. Reorganization of cerebral networks after stroke: New insights
960 from neuroimaging with connectivity approaches. *Brain* **134**, 1264–1276 (2011).

961 44. Grefkes, C. & Fink, G. R. Connectivity-based approaches in stroke and recovery of
962 function. *Lancet Neurol.* **13**, 206–216 (2014).

963 45. Chung, D. Y. *et al.* Subarachnoid hemorrhage leads to early and persistent functional
964 connectivity and behavioral changes in mice. *J. Cereb. Blood Flow Metab.* **41**, 975–985
965 (2021).

966 46. Kura, S. *et al.* Intrinsic optical signal imaging of the blood volume changes is sufficient
967 for mapping the resting state functional connectivity in the rodent cortex. *J. Neural Eng.* **c**,
968 (2018).

969 47. Xie, H. *et al.* Differential effects of anesthetics on resting state functional connectivity in
970 the mouse. *J. Cereb. Blood Flow Metab.* **40**, 875–884 (2020).

971 48. Angels Font, M., Arboix, A. & Krupinski, J. Angiogenesis, Neurogenesis and
972 Neuroplasticity in Ischemic Stroke. *Curr. Cardiol. Rev.* **6**, 238–244 (2010).

973 49. Boyd, L. A. *et al.* Biomarkers of stroke recovery: Consensus-based core recommendations
974 from the Stroke Recovery and Rehabilitation Roundtable. *Int. J. Stroke* **12**, 480–493
975 (2017).

976 50. Stinear, C. M. Prediction of motor recovery after stroke: advances in biomarkers. *Lancet*
977 *Neurol.* **16**, 826–836 (2017).

978 51. Rabiller, G., He, J. W., Nishijima, Y., Wong, A. & Liu, J. Perturbation of brain
979 oscillations after ischemic stroke: A potential biomarker for post-stroke function and
980 therapy. *Int. J. Mol. Sci.* **16**, 25605–25640 (2015).

981 52. Huang, M. X. *et al.* Marked Increases in Resting-State MEG Gamma-Band Activity in
982 Combat-Related Mild Traumatic Brain Injury. *Cereb. Cortex* **30**, 283–295 (2020).

983 53. Intaglietta, M. Arteriolar Vasomotion: Implications for Tissue Ischemia. *J. Vasc. Res.*
984 **28(suppl 1)**, 1–7 (1991).

985 54. Intaglietta, M. Vasomotion and flowmotion: physiological mechanisms and clinical
986 evidence. *Vasc. Med. Rev.* **vmr-1**, 101–112 (1990).

987 55. Carmichael, S. T. Brain excitability in stroke: The yin and yang of stroke progression.
988 *Arch. Neurol.* **69**, 161–167 (2012).

989 56. Joy, M. T. & Carmichael, S. T. Encouraging an excitable brain state: mechanisms of brain
990 repair in stroke. *Nat. Rev. Neurosci.* **22**, 38–53 (2021).

991 57. Bütfisch, C. M., Netz, J., Weßling, M., Seitz, R. J. & Hömberg, V. Remote changes in
992 cortical excitability after stroke. *Brain* **126**, 470–481 (2003).

993 58. Mohajerani, M. H., Aminoltejari, K. & Murphy, T. H. Targeted mini-strokes produce
994 changes in interhemispheric sensory signal processing that are indicative of disinhibition
995 within minutes. *Proc. Natl. Acad. Sci.* **108**, E183–E191 (2011).

996 59. Balbi, M. *et al.* Gamma frequency activation of inhibitory neurons in the acute phase after
997 stroke attenuates vascular and behavioral dysfunction. *Cell Rep.* **34**, 108696 (2021).

998 60. Adaikkan, C. *et al.* Gamma Entrainment Binds Higher-Order Brain Regions and Offers
999 Neuroprotection. *Neuron* **102**, 929–943.e8 (2019).

1000 61. Rehme, A. K., Eickhoff, S. B., Wang, L. E., Fink, G. R. & Grefkes, C. Dynamic causal
1001 modeling of cortical activity from the acute to the chronic stage after stroke. *Neuroimage*
1002 **55**, 1147–1158 (2011).

1003 62. Rehme, A. K., Eickhoff, S. B., Rottschy, C., Fink, G. R. & Grefkes, C. Activation
1004 likelihood estimation meta-analysis of motor-related neural activity after stroke.
1005 *Neuroimage* **59**, 2771–2782 (2012).

1006 63. Carmichael, S. T. & Chesselet, M. F. Synchronous neuronal activity is a signal for axonal
1007 sprouting after cortical lesions in the adult. *J. Neurosci.* **22**, 6062–6070 (2002).

1008 64. White, B. R. *et al.* Imaging of functional connectivity in the mouse brain. *PLoS One* **6**,
1009 (2011).

1010 65. Isaacson, J. S. & Scanziani, M. How inhibition shapes cortical activity. *Neuron* **72**, 231–
1011 243 (2011).

1012 66. Hamel, E. Perivascular nerves and the regulation of cerebrovascular tone. *J. Appl. Physiol.*
1013 **100**, 1059–1064 (2006).

1014 67. Attwell, D. *et al.* Glial and neuronal control of brain blood flow. *Nature* **468**, 232–243
1015 (2010).

1016 68. Lo, E. H., Dalkara, T. & Moskowitz, M. A. Neurological diseases: Mechanisms,
1017 challenges and opportunities in stroke. *Nat. Rev. Neurosci.* **4**, 399–414 (2003).

1018 69. Sunil, S. *et al.* Awake chronic mouse model of targeted pial vessel occlusion via
1019 photothrombosis. *Neurophotonics* **7**, 1–18 (2020).

1020 70. Kim, T. H. *et al.* Long-Term Optical Access to an Estimated One Million Neurons in the
1021 Live Mouse Cortex. *Cell Rep.* **17**, 3385–3394 (2016).

1022 71. Dunn, A. K., Devor, A., Dale, A. M. & Boas, D. A. Spatial extent of oxygen metabolism
1023 and hemodynamic changes during functional activation of the rat somatosensory cortex.
Neuroimage **27**, 279–290 (2005).

1025 72. Fang, Q. & Boas, D. A. Monte Carlo Simulation of Photon Migration in 3D Turbid Media
1026 Accelerated by Graphics Processing Units. *Opt. Express* **17**, 20178 (2009).

1027 73. Chen, J., Fang, Q. & Intes, X. Mesh-based Monte Carlo method in time-domain widefield
1028 fluorescence molecular tomography. *J. Biomed. Opt.* **17**, 1 (2012).

1029 74. Sunil, S. *et al.* NeuroImage : Clinical Stroke core revealed by tissue scattering using
1030 spatial frequency domain imaging. *NeuroImage Clin.* **29**, 102539 (2021).

1031 75. Srinivasan, V. J. *et al.* Multiparametric, Longitudinal Optical Coherence Tomography
1032 Imaging Reveals Acute Injury and Chronic Recovery in Experimental Ischemic Stroke.
PLoS One **8**, (2013).

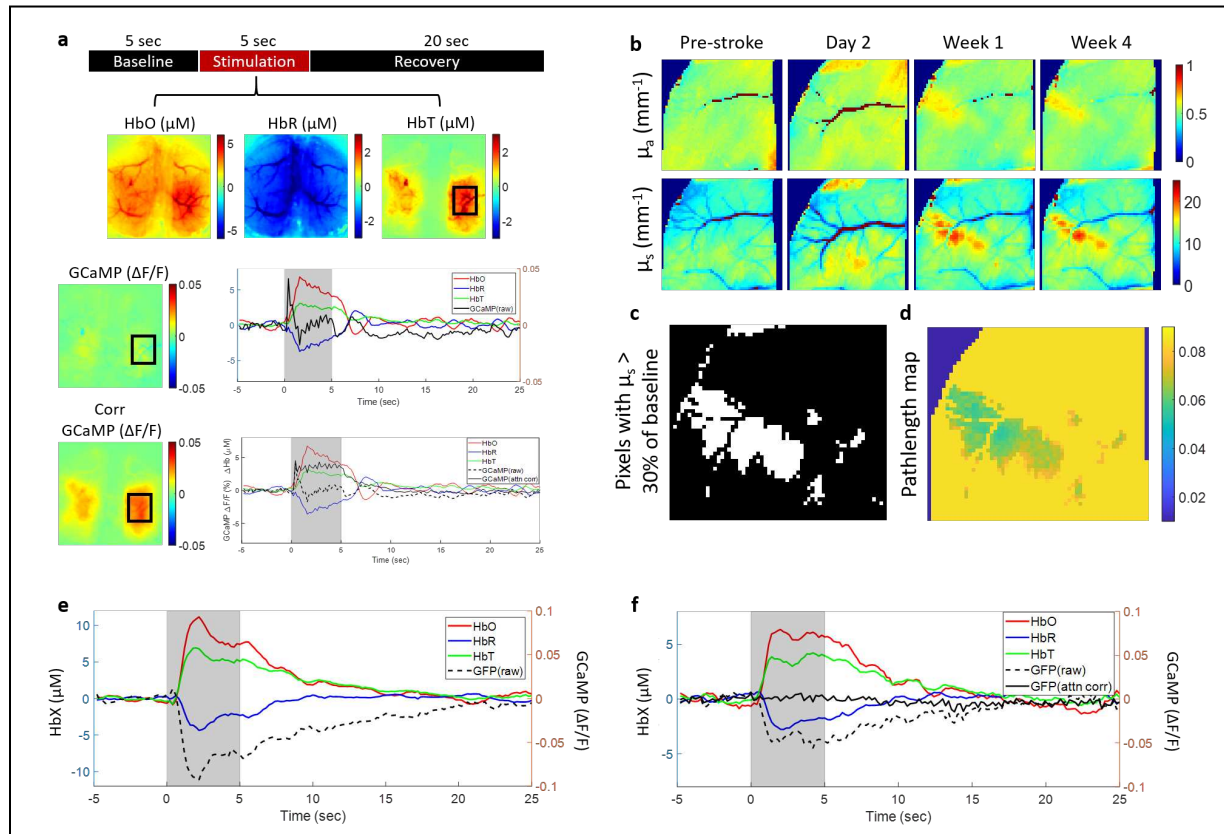
1034

1035 **Supplementary Material**

1036

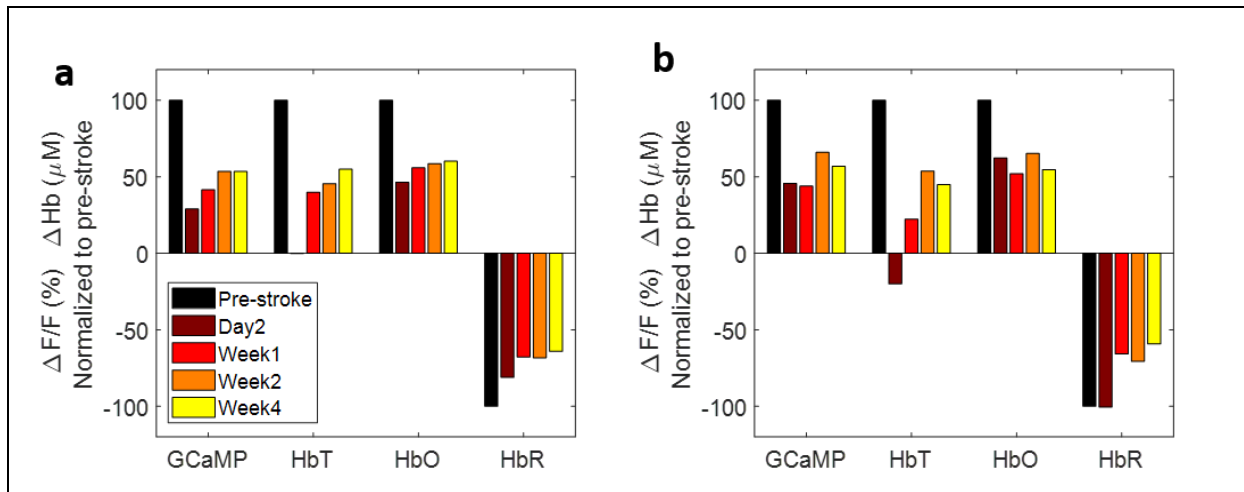
1037 *Supplementary Figures*

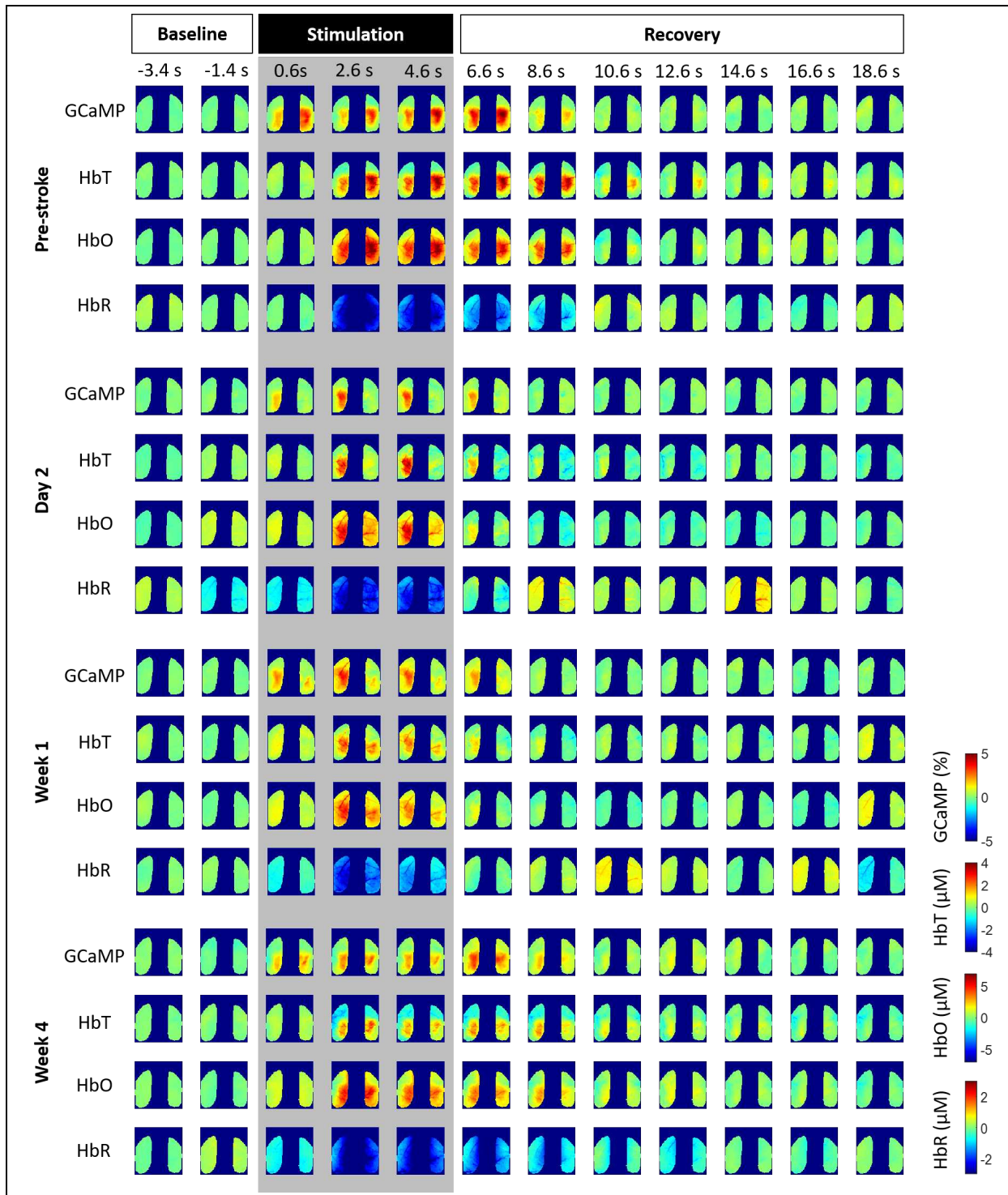
1038



1040 **Supplementary figure 1:** Fluorescence correction for hemodynamic crosstalk. (a) Top: Block
 1041 design of single sensory stimulation trial and spatial hemodynamic response maps for HbO, HbR,
 1042 and HbT. Middle: Raw GCaMP response map during 5 sec of sensory stimulation and time course
 1043 of trial averaged data for GCaMP and hemodynamics from ROI marked in black box. Uncorrected
 1044 GCaMP shows rise in fluorescence at the start of stimulation but begins to decrease with the rise
 1045 of hemodynamic response. Bottom: Spatial map of GCaMP corrected for hemodynamic crosstalk.
 1046 Note the appearance of response compared to uncorrected GCaMP in spatial map. Time course of
 1047 corrected GCaMP overlaid with uncorrected GCaMP and hemodynamics. Note that GCaMP is
 1048 now elevated for the full stimulation period. (b) Absorption and scattering coefficients obtained
 1049 from SFDI before and after stroke and used in the correction algorithm in the form of pathlength
 1050 factor. Stroke leads to increases in the scattering signal that needs to be accounted for accurate
 1051 correction due to its effect on pathlength. (c) Binary maps of all pixels that have scattering
 1052 coefficient greater than 30% of baseline scattering. The scattering and absorption coefficients from
 1053 these pixels are used in the Monte Carlo simulation to obtain pathlength. (d) Spatial map of
 1054 pathlength factors obtained from Monte Carlo simulations and used in the correction algorithm.
 1055 (e,f) Validation of correction algorithm with cellular fluorescent marker GFP. (e) GFP signal
 1056 overlaid with hemodynamics during 5sec of sensory stimulation. GFP drops in association with

1057 hemodynamic increase. (f) Correction applied to GFP signal during sensory stimulation. Corrected
1058 GFP is a flat line as expected since GFP fluorescence is not altered with neural activity or
1059 hemodynamics.



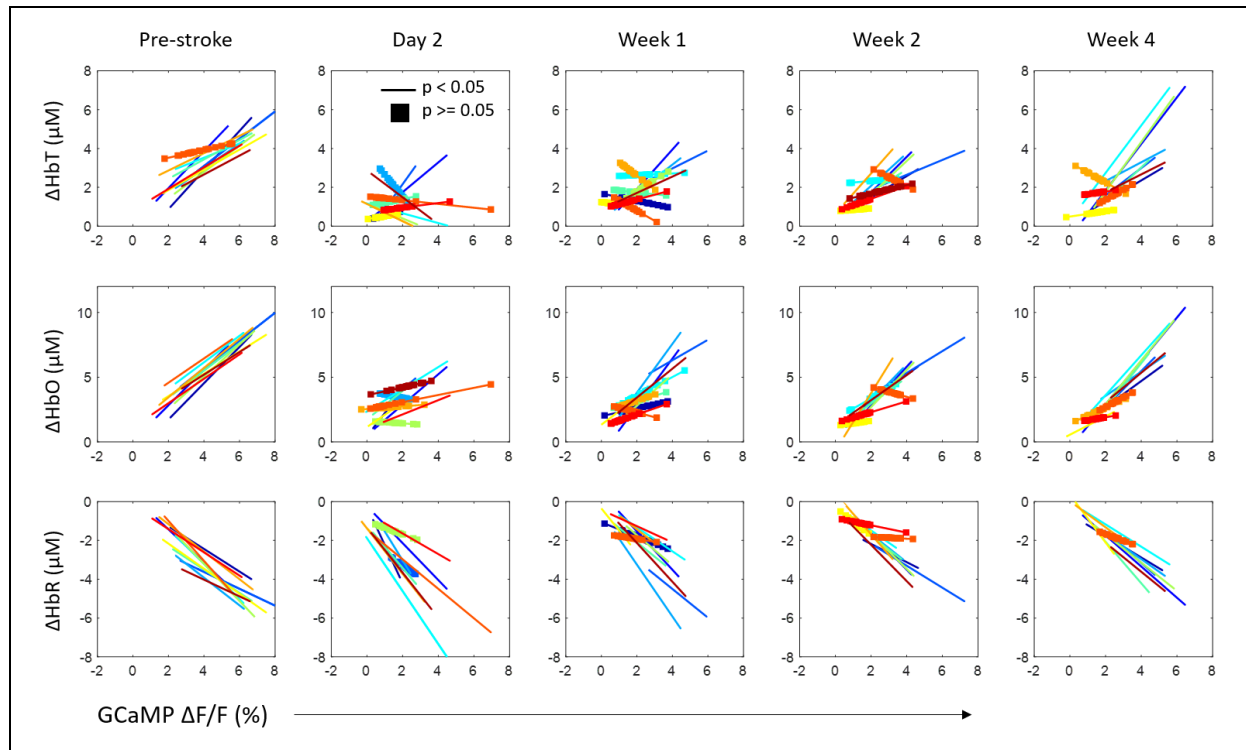


1065

1066

1068

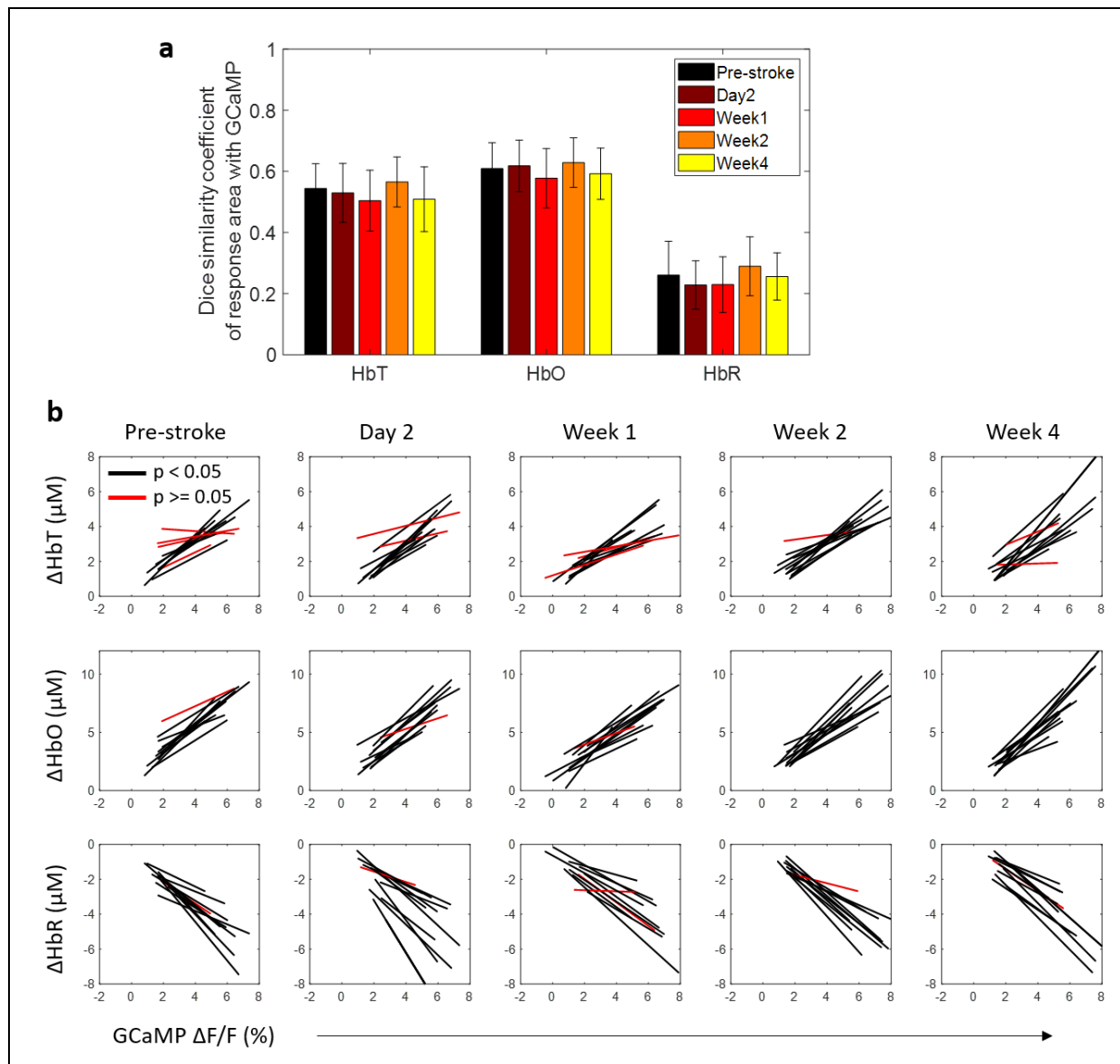
Supplementary figure 3: Spatial maps of GCaMP and hemodynamic responses over time during sensory stimulation.



1069

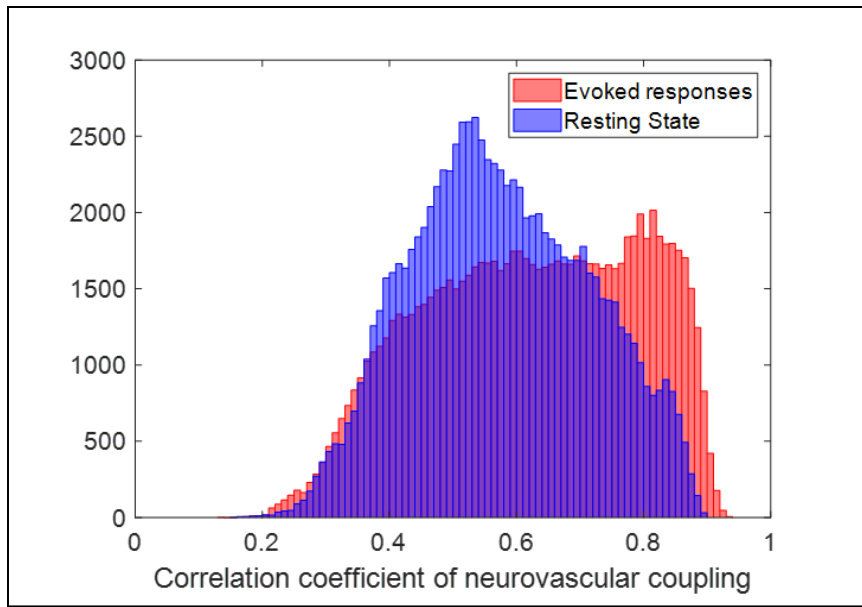
1070 **Supplementary figure 4:** Correlation of calcium and hemodynamic evoked responses to sensory
1071 stimulation of the affected forelimb color-coded by mouse. Mice with significant correlation in
1072 response magnitudes of calcium and hemodynamics are shown as solid lines and mice whose
1073 responses were not correlated are shown with filled squares. Note that the animals that did not
1074 show correlation at week 4 after stroke also lacked correlation in the acute phase of stroke at week
1075 1.

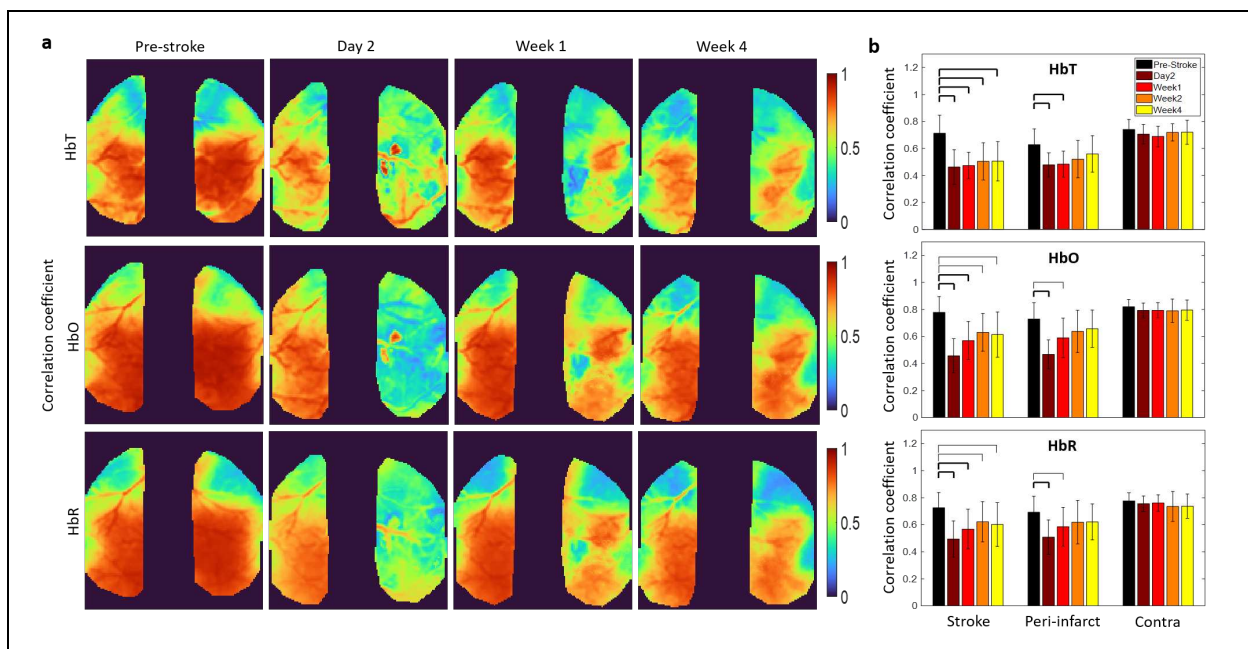
1076



1078 **Supplementary figure 5:** Responses within the unaffected hemisphere during stimulation of the
1079 unaffected forelimb. (a) Dice similarity coefficient between GCaMP response areas with each
1080 hemodynamic measure. There was no change in similarity of response area after stroke. (b)
1081 Correlation of calcium and hemodynamic evoked responses in the unaffected forelimb to sensory
1082 stimulation of the unaffected forelimb.

1083

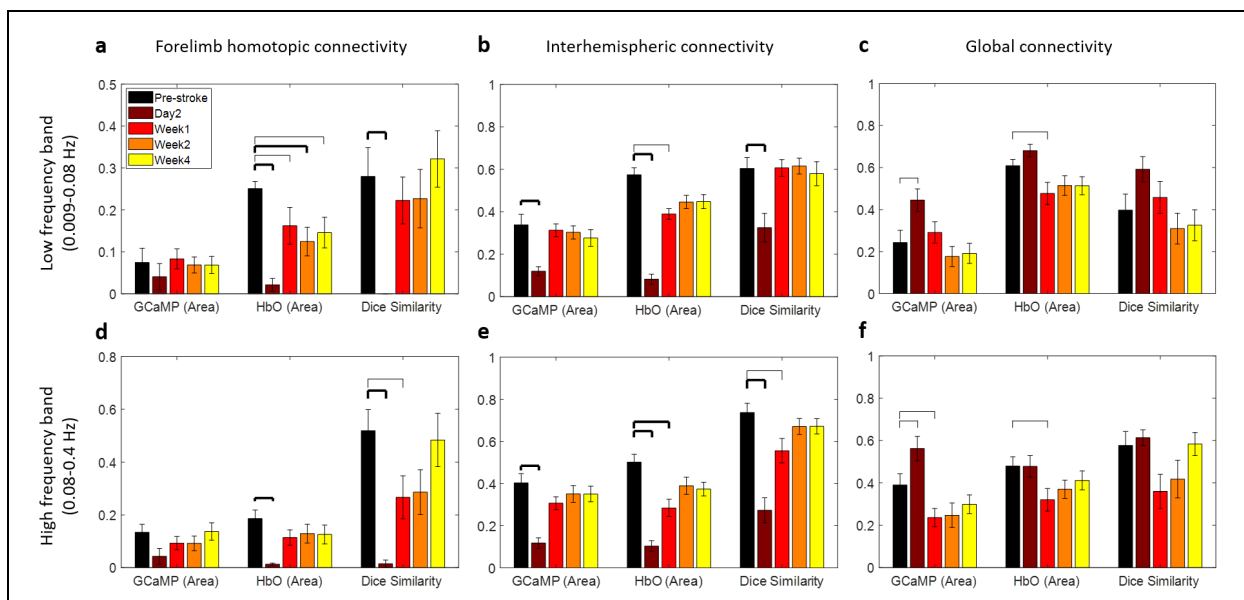




1088

1089 **Supplementary figure 7:** (a) Pixel-by-pixel Pearson's correlation coefficient between measured
1090 and predicted HbT (top), HbO (middle), and HbR (bottom). Predicted HbX is obtained by
1091 convolving the GCaMP signal at each time point with the HRF obtained for that specific time point
1092 and pixel. (b) Pearson's correlation coefficient quantified across all mice within the stroke core,
1093 peri-infarct, and contralateral forelimb region. Thick bars: $p < 0.01$, thin bars: $p < 0.05$.

1094



1095

1096 **Supplementary figure 8:** RSFC proportional area and dice coefficient analysis at threshold of
1097 0.4. Each figure shows the proportional area of GCaMP and HbO above the correlation coefficient
1098 equal to 0.4 and the dice similarity between the GCaMP and HbO at 0.4. (a) Forelimb homotopic
1099 connectivity in the low frequency band and (d) high frequency band. (b) Interhemispheric
1100 connectivity in the low frequency band and (e) high frequency band. (c) Global connectivity in the
1101 low frequency band and (f) high frequency band.

1102